JACS Au
AN OPEN ACCESS JOURNAL OF THE AMERICAN CHEMICAL SOCIETY

Machine Learning Reveals Amine Type in Polymer Micelles Determines mRNA Binding, *In Vitro, and In Vivo* Performance for Lung-Selective Delivery

Sidharth Panda, Ella J. Eaton, Praveen Muralikrishnan, Erin M. Stelljes, Davis Seelig, Michael C. Leyden, Alexandria K. Gilkey, Jackson T. Barnes, David V. Morrissey, Sapna Sarupria, Branden S. Moriarity, and Theresa M. Reineke*

Cite This: *JACS Au* 2025, 5, 1845−1861

Read Online

ACCESS | Metrics & More | Article Recommendations | Supporting Information

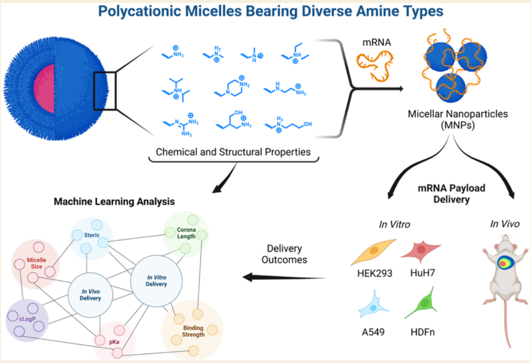

ABSTRACT: Cationic micelles, composed of amphiphilic block copolymers with polycationic coronas, offer a customizable platform for mRNA delivery. Here, we present a library of 30 cationic micelle nanoparticles (MNPs) formulated from diblock copolymers with reactive poly(pentafluorophenol acrylate) backbones modified with diverse amines. This library systematically varies in nitrogen-based cationic functionalities, exhibiting a spectrum of properties that encompass varied degrees of alkyl substitution (A1−A5), piperazine (A6), oligoamine (A7), guanidinium (A8), and hydroxylation (A9−A10) that vary in side-chain volume, substitution pattern, hydrophilicity, and pK_a to assess parameter impact on mRNA delivery. *In vitro* delivery assays using GFP+ mRNA across multiple cell lines reveal that amine side-chain bulk and chemical structure critically affect performance. Using machine learning analysis via SHapley Additive exPlanations (SHAP) on 180 formulations (3780 experimental measurements), we mapped key relationships between amine chemistry and performance metrics, finding that amine-specific binding efficiency was a major determinant of mRNA delivery efficacy, cell viability, and GFP intensity. Micelles with stronger mRNA binding capabilities (A1 and A7) have higher cellular delivery performance, whereas those with intermediate binding tendencies deliver a higher amount of functional mRNA per cell (A2, A10). This indicates that balancing the binding strength is crucial for performance. Micelles with hydrophobic and bulky pendant groups (A3−A5) tend to induce necrosis during cellular delivery, highlighting the significance of chemical optimization. A7 amphiphile, displaying primary and secondary amine, consistently demonstrates the highest GFP expression across various cell types and *in vivo* achieves high delivery specificity to lung tissue upon intravenous administration. Moreover, we established a strong correlation between *in vitro* and *in vivo* performance using Multitask Gaussian Process models, underscoring the predictive power of *in vitro* models for anticipating *in vivo* outcomes. Overall, this innovative study integrates advanced data science with experimental design, demonstrating the pivotal role of chemical amine-dependent optimization for advancing targeted mRNA delivery to the lungs.

KEYWORDS: *mRNA delivery, polymer, amphiphile, lung tropism, micelle*

INTRODUCTION

Nucleic acid therapeutics leverage precise modulation of the cellular genome and proteome, offering immense potential for treating numerous acquired and inherited diseases from thalassemia and sickle cell anemia to cystic fibrosis and cancer.[1−3] Unprecedented human health advancements are being realized via 26 FDA-approved genetic medicines and over 3000 ongoing clinical trials via *ex vivo* and *in vivo* delivery of nucleic acids into cells and tissues.[4] Messenger RNA (mRNA) has been globally applied in vaccines and numerous clinical trials due to its ability to express therapeutic proteins without the need for nuclear translocation and lower risk of genotoxicity and mutagenesis.[5,6] However, mRNAs are rapidly degraded by RNases and show low stability and poor cellular uptake. Viral nanoparticles and lipid nanoparticles (LNPs) have been proven in the clinic for mRNA delivery.[7,8] However, thermal stability concerns for LNPs[9,10] alongside astronomical manufacturing costs and inflammatory response from viruses[11,12] have fostered exploration and discovery of alternate delivery systems. Polymer-based vehicles offer an exceptionally vast synthetic design space, facile composition modularity, and well-defined

Received: January 23, 2025
Revised: March 19, 2025
Accepted: March 20, 2025
Published: April 14, 2025

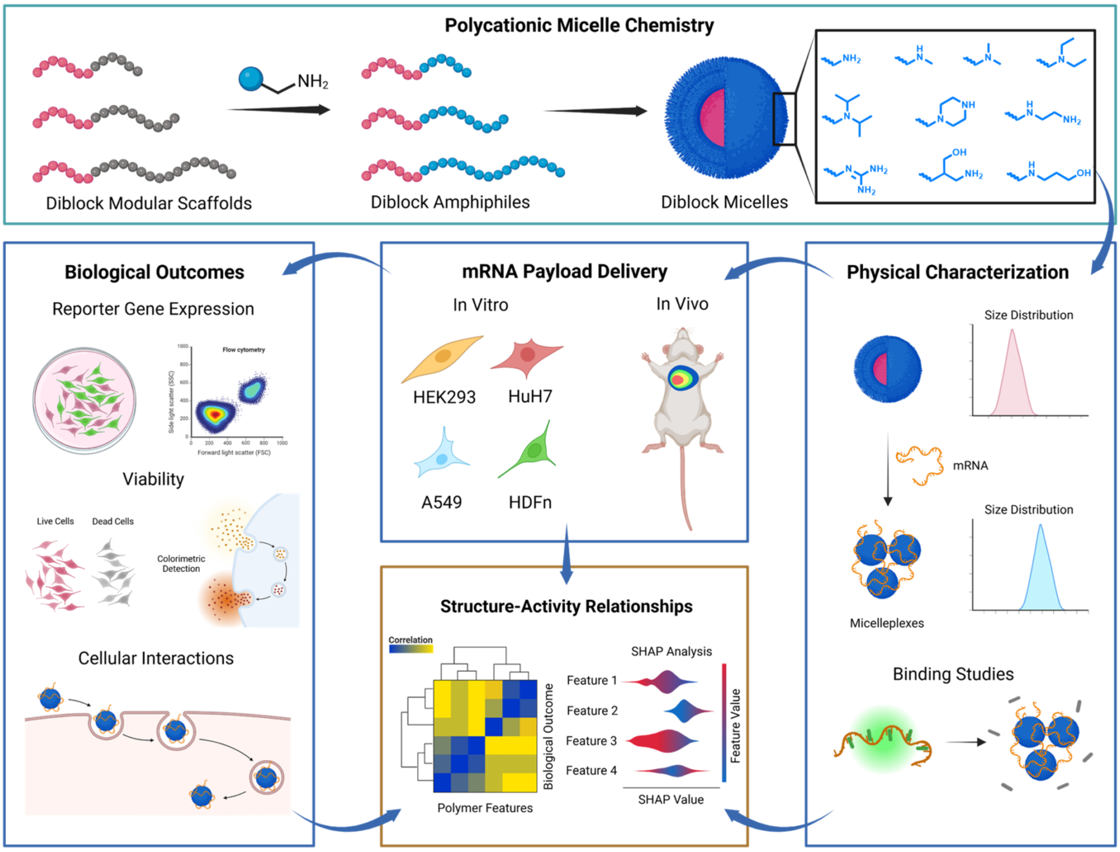

Figure 1. Generation of diblock cationic amphiphiles from diblock modular scaffolds via postpolymerization modification. The subsequently formulated micelles were complexed with mRNA, biophysically characterized, and screened via *in vitro* and *in vivo* assays to determine the delivery performance. The biological performance was evaluated via SHAP analysis and allied statistical tools to elucidate micelle−mRNA structure−activity *in vitro*/*in vivo* performance relationships.

architecture as alternative nucleic acid delivery vehicles. This, coupled with decades of research and development optimizing low-cost production on mass scale, offers unprecedented opportunities for tailoring vehicle design.[13,14] Polymer vehicles provide a new avenue for the exploration of novel vector architectures and chemistries for mRNA delivery that previously remained inaccessible through viral and LNP vector systems, yet coupling the physicochemical structure, biological properties, and *in vivo* performance is still in the early stages of development.

Cationic polymers such as poly(ethylenimine) (PEI)[15−18] and poly(dimethylaminoethyl methacrylate) (PDMAEMA)[19−21] are the predominant polymeric delivery systems due to their ability to form electrostatic complexes with negatively charged nucleic acids. Various polymer architectures, including homopolymers, alternating and statistical copolymers, block copolymers, as well as branched, star, and brush-like structures, have shown effective packaging of nucleic acids into complexes commonly referred to as polyplexes, polyelectrolyte complexes (PECs), and polymer nanoparticles (PNPs).[13] These complexes are known to facilitate efficient intracellular delivery. Among these, assemblies of amphiphilic block copolymers bearing pendant polycationic coronas, known as micelles, have emerged as a promising class of polycationic delivery systems in drug and nucleic acid delivery.[22−25] Micelles offer structural similarities to both LNPs and PNPs (Figure 1) via a marriage of unlimited chemical modification, formulation composition, and uniform preassembled particle sizes. When complexed with nucleic acids, these micelles form micellar nanoparticles (MNPs) or micelleplexes. Our group has shown that MNPs provide a well-defined paradigm providing multivalent cationic corona for binding of polyanionic payloads. Micelles and MNPs benefit from extremely slow chain-exchange kinetics and enhanced compaction of nucleic acid cargo, which ensures better colloidal stability and delivery efficiency.[26−28] Furthermore, our group has shown that self-assembled micelles have demonstrated superior delivery performance compared to their linear counterparts for various nucleic acid payloads, including plasmid DNA (pDNA) and antisense oligonucleotides (ASOs).[29−32]

Multiple investigations have shown that variations in the chemistry, morphology, and formulation of polycationic micelles significantly affect the complexation and delivery efficiency of pDNA, Cas9 ribonucleoprotein, and siRNAs.[33−37] For example, Duvall et al. showed that modifying the corona charge density by mixing neutral poly(ethylene glycol) (PEG)-based amphiphiles with DMAEMA based cationic amphiphiles improved siRNA unpackaging and significantly impacted *in vivo* biodistribution.[35] Similarly, Traeger et al. were able to improve pDNA delivery efficiency in cultured cells and MNP stability in serum by reducing cationic charge density via the incorporation of anionic functionalities.[34] Importantly, these findings suggest that the charge−charge interactions between the polycation and nucleic acid payload dictate the formation of micelleplexes and their subsequent disassembly, thus critically impacting the delivery performance. Nitrogenous moieties are the conventional archetype of cationic moieties used in the design of

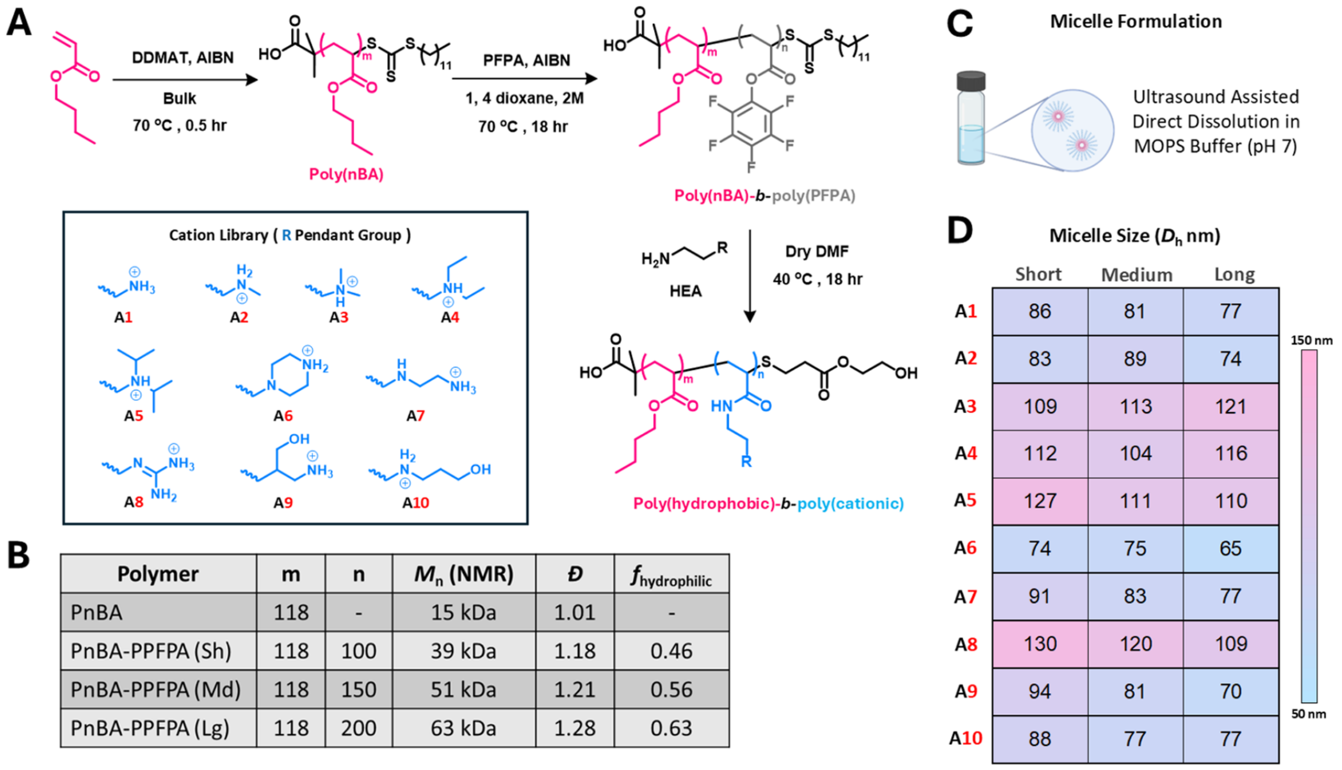

Polymer	m	n	M_n (NMR)	$Đ$	$f_{hydrophilic}$
PnBA	118	-	15 kDa	1.01	-
PnBA-PPFPA (Sh)	118	100	39 kDa	1.18	0.46
PnBA-PPFPA (Md)	118	150	51 kDa	1.21	0.56
PnBA-PPFPA (Lg)	118	200	63 kDa	1.28	0.63

	Short	Medium	Long
A1	86	81	77
A2	83	89	74
A3	109	113	121
A4	112	104	116
A5	127	111	110
A6	74	75	65
A7	91	83	77
A8	130	120	109
A9	94	81	70
A10	88	77	77

Figure 2. (A) Scheme for the synthesis of diblock scaffolds via RAFT polymerization and their subsequent modification with a library of 10 different cationic modifiers. (B) Diblock scaffold characterization via ^{1}H NMR ($CDCl_3$ solvent) and SEC-MALS (THF solvent) showed the parent hydrophobic block and three modifiable block lengths. (C) Micelle formulation in MOPS buffer and (D) micelle size characterization via DLS. Sh/Short, Md/Medium, and Lg/Long indicate short, medium, and long corona amphiphile, respectively.

polycationic delivery vehicles. Our group has previously reported that amine structure can alter *in vitro* performance in studies led by Santa Chalarca et al. for micelle-pDNA systems[31] and Hanson et al. for micelle-ASO systems.[32] However, despite the availability of large design space, micellar delivery systems have mostly been limited to PDMAEMA-based scaffolds with some micelle-like structures being studied based on modified PEI.[13,14] These amine-type-based dependencies have been observed for a variety of different nucleic acids. However, a cohesive head-to-head assessment correlating cationic micelle physicochemical properties with mRNA complexation and delivery performance *in vitro* and *in vivo* is still lacking, hindering further clinical development of this novel, stable, and scalable MNP high-performance vehicle class.

In addition to driving mRNA complexation kinetics, the identity of charged groups in nanoparticle formulations can significantly influence biodistribution and *in vivo* performance[38−40] The cationic charge imparted by these amines can lead to protein opsonization, resulting in serum fouling and reduced delivery efficacy. However, by altering the nanoparticle surface chemistry, it is possible to recruit specific serum proteins that facilitate targeted delivery to extrahepatic organs.[41] For instance, research on lipid nanoparticles (LNPs) has advanced this field, with Siegwart et al. demonstrating Selective Organ Targeting (SORT) LNPs.[42] By tuning the helper lipid within a five-component lipid formulation, they achieved targeted delivery of mRNA to organs such as the liver, lungs, and spleen. Studies also suggest that nanocarriers containing quaternary ammonium moieties can effectively target the lungs via intravenous administration.[43−45] However, nontitratable amines like quaternary ammonium groups often exhibit poor nucleic acid cargo release,[22,23,46−48] necessitating the use of charge density-reducing helper lipids or comonomers to enhance performance. While these laborious empirical strategies provide information, their fiscally intensive synthesis, characterization, formulation, and biological testing efforts are limiting. Thus, there is a dire need to develop intelligent structure discovery and efficiency correlations via data science methods to rapidly improve predictive nucleic acid delivery performance with well-defined formulations.

In this work, we identify the fundamental physicochemical properties of cationic micelles that dictate their efficacy for mRNA delivery *in vitro* and *in vivo*, with the goal of guiding future generations of optimized organ tropic formulations for polymer vehicles (Figure 1). We hypothesize that amine chemistry/identity, pK_a/pH responsiveness, molecular volume, and hydrophilic/hydrophobic balance all play key roles in altering *in vitro* or *in vivo* performance and tropism. To test this hypothesis, we developed a streamlined parallel workflow to generate modifiable diblock polymers yielding 30 micelle structures and thousands of experimental data points, leveraging the heuristic tools of parallel synthesis/characterization and machine learning. *In vitro* delivery experiments using GFP-encoding mRNA with various cell lines were conducted to assess the delivery efficiency. A machine learning method based on SHapley Additive exPlanations (SHAP) analysis was employed to correlate and decipher key design principles that dictate performance. Indeed, the chemical properties of the amines significantly impact performance. Micelles with strong mRNA binding capabilities yield higher cellular delivery performance, those with intermediate binding deliver a higher amount of mRNA per cell, and structures with hydrophobic/bulky pendant

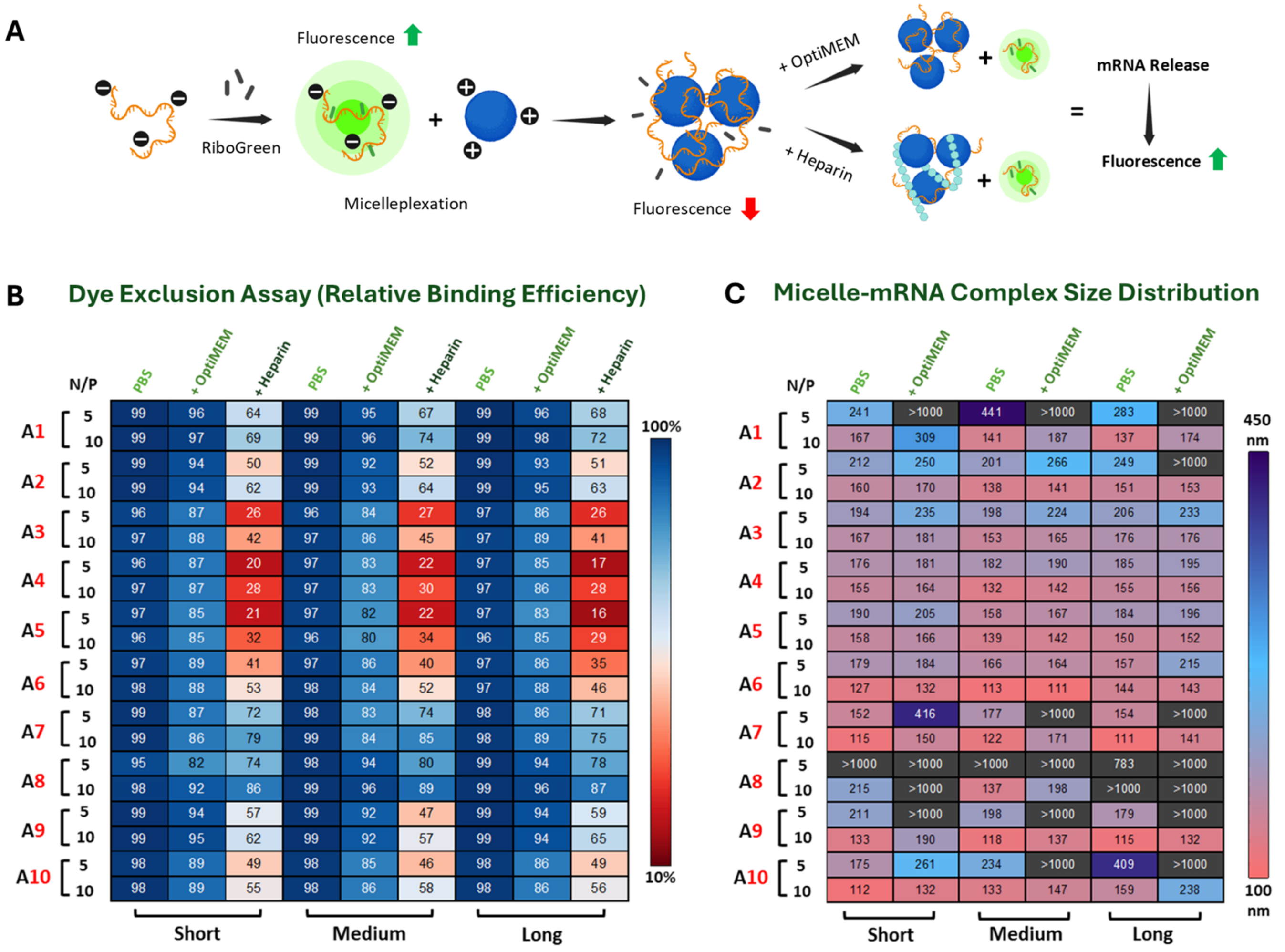

B Dye Exclusion Assay (Relative Binding Efficiency)

	N/P	Short PBS	Short + OptiMEM	Short + Heparin	Medium PBS	Medium + OptiMEM	Medium + Heparin	Long PBS	Long + OptiMEM	Long + Heparin
A1	5	99	96	64	99	95	67	99	96	68
	10	99	97	69	99	96	74	99	98	72
A2	5	99	94	50	99	92	52	99	93	51
	10	99	94	62	99	93	64	99	95	63
A3	5	96	87	26	96	84	27	97	86	26
	10	97	88	42	97	86	45	97	89	41
A4	5	96	87	20	97	83	22	97	85	17
	10	97	87	28	97	83	30	97	86	28
A5	5	97	85	21	97	82	22	97	83	16
	10	96	85	32	96	80	34	96	85	29
A6	5	97	89	41	97	86	40	97	86	35
	10	98	88	53	98	84	52	97	88	46
A7	5	99	87	72	98	83	74	98	86	71
	10	99	86	79	99	84	85	98	89	75
A8	5	95	82	74	98	94	80	99	94	78
	10	98	92	86	99	96	89	99	96	87
A9	5	99	94	57	99	92	47	99	94	59
	10	99	95	62	99	92	57	99	94	65
A10	5	98	89	49	98	85	46	98	86	49
	10	98	89	55	98	86	58	98	86	56

C Micelle-mRNA Complex Size Distribution

	N/P	Short PBS	Short + OptiMEM	Medium PBS	Medium + OptiMEM	Long PBS	Long + OptiMEM
A1	5	241	>1000	441	>1000	283	>1000
	10	167	309	141	187	137	174
A2	5	212	250	201	266	249	>1000
	10	160	170	138	141	151	153
A3	5	194	235	198	224	206	233
	10	167	181	153	165	176	176
A4	5	176	181	182	190	185	195
	10	155	164	132	142	155	156
A5	5	190	205	158	167	184	196
	10	158	166	139	142	150	152
A6	5	179	184	166	164	157	215
	10	127	132	113	111	144	143
A7	5	152	416	177	>1000	154	>1000
	10	115	150	122	171	111	141
A8	5	>1000	>1000	>1000	>1000	783	>1000
	10	215	>1000	137	198	>1000	>1000
A9	5	211	>1000	198	>1000	179	>1000
	10	133	190	118	137	115	132
A10	5	175	261	234	>1000	409	>1000
	10	112	132	133	147	159	238

Figure 3. (A) Scheme representation of micelleplex formation and dye exclusion assay to determine the mRNA binding efficiency of the micelles. (B) Micelle−mRNA binding efficiency in PBS (micelleplex formulation media), OptiMEM (transfection media), and heparan (to demonstrate mRNA release efficiency from the micelleplexes).(C) Micelleplex size (D_h, nm) characterization via DLS measurements.

groups induce necrosis during cellular delivery. Notably, a pH-responsive amphiphile with a polyamine-based pendant moiety, designated A7, emerged as the top performer, exhibiting exemplary delivery efficiency across cell lines. Using Multitask Gaussian Process models, *in vitro* and *in vivo* data correlation is shown linking amine properties directly to both delivery efficacy and biodistribution. Overall, this work is the first to show that cationic polymers can be tailored to yield both exceptional performance and lung-selective targeting via intravenous (IV) administration. These findings highlight the critical role of amine-based functional group design in optimizing the physicochemical properties of cationic micelles for mRNA delivery. This work integrates advanced data science tools into a robust synthetic and characterization framework for the rational design of next-generation, organ-specific mRNA delivery systems, paving the way for more effective, affordable, and targeted mRNA therapeutics.

RESULTS AND DISCUSSION

Polymer Amphiphile Synthesis, Micelle Formation, and Characterization

Postpolymerization functionalization of reactive polymer scaffolds provides a facile avenue for the combinatorial synthesis of polymer libraries.[49,50] This methodology addresses challenges associated with monomer incompatibility arising from differing reactivity ratios, a limitation often constraining accessible polymer sequences. In the current study, we synthesize a set of postpolymerization modifiable diblock copolymer scaffolds, with poly(*n*-butyl acrylate) serving as the hydrophobic block and poly(pentafluorophenol acrylate) as the modular block. To understand the effect of corona cation density on mRNA binding and delivery, we introduce variability in the molecular weight of pentafluorophenol acrylate via chain extension on a PnBA block, generating three distinct parent modular scaffolds (Figure 2A,B). Previous research has established that for diblock polymers, a hydrophilic fraction ($f_{\text{hydrophilic}}$) of approximately 0.5 is indicative of spherical micelle formation.[51,52] In our three parent polymer scaffolds, the PnBA block (hydrophobic) is kept constant at 118 repeat units (RU), while the modular block is varied with lengths of 100 repeat units (RU) (Short Library, 0.46 $f_{\text{hydrophilic}}$), 150 RU (Medium Library, 0.56 $f_{\text{hydrophilic}}$), and 200 RU (Long Library, 0.63 $f_{\text{hydrophilic}}$) (Figures 2A,B and S3).

We then reacted each scaffold with 10 different primary amine-based modifiers to readily yield a series of 30 poly(nBA)-*b*-poly(cation) copolymers with a focus on acrylamide linkers for stability and performance.[53] The primary amine modifiers feature nitrogen-based cationic functionalities, exhibiting a spectrum of properties that encompass varied degrees of alkyl

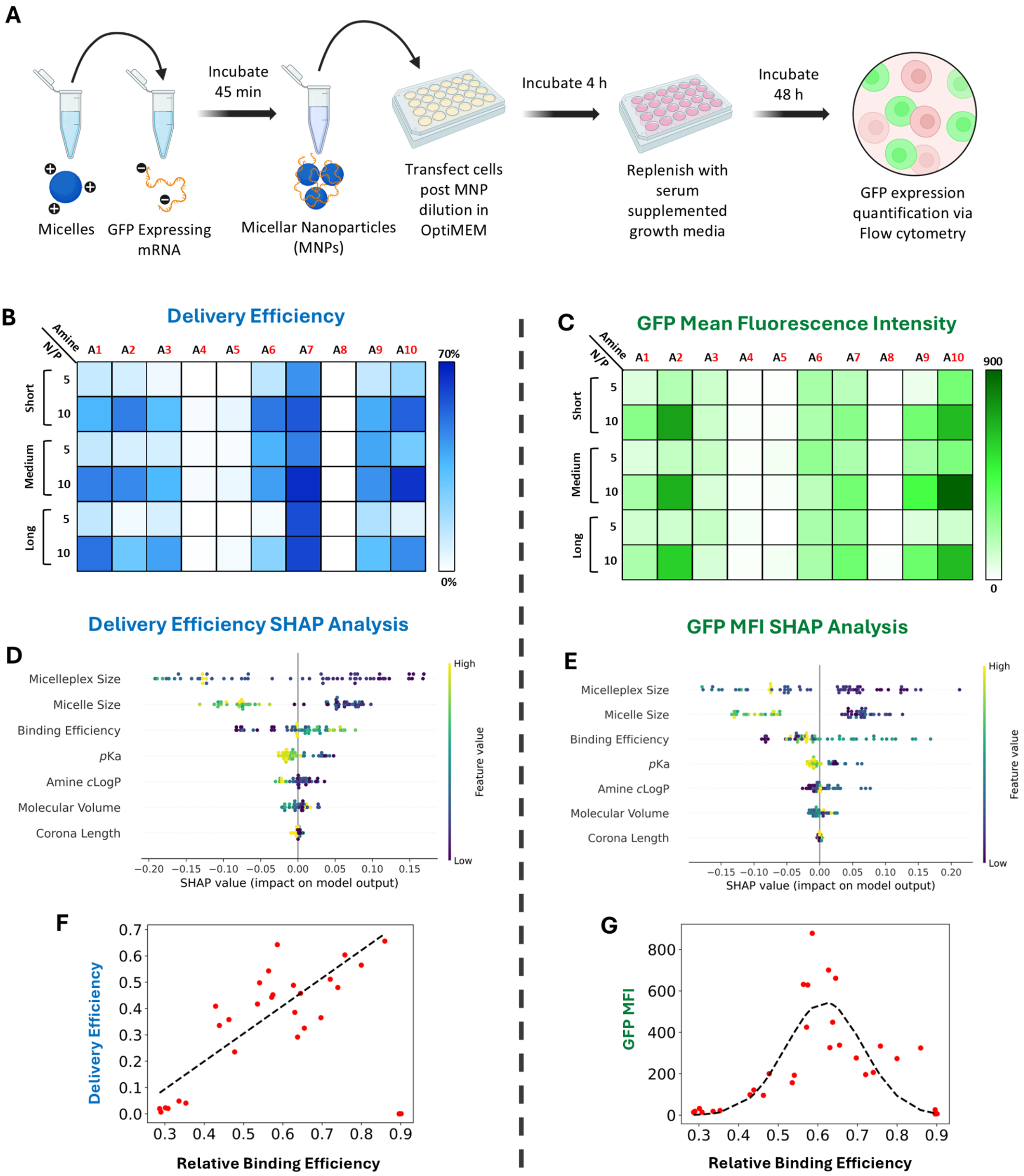

Figure 4. (A) Scheme for general *in vitro* transfection. GFP expressing mRNA is used to prepare micelleplexes that are transfected in HEK293T cells, followed by quantification of GFP-positive cells via flow cytometry. Heatmap showcasing (B) transfection efficiency (% of cells GFP-positive) and (C) mean fluorescence intensity of GFP expression (GFP MFI) of the full micelle library upon transfection in HEK293T cells. SHAP plots for (D) *in vitro* transfection efficiency (serum-free), (E) *in vitro* GFP mean fluorescence intensity. For SHAP plots, each chemical and physical feature is the input, and the biological performance is the output; the feature importance is indicated by the SHAP value magnitude, and the sign denotes the correlation with the model output. Plots showing dependency of (F) transfection efficiency and (G) GFP mean fluorescence intensity on relative binding efficiency.

substitution (A1−A5), hydroxylation (A9−A10), and include specialty amines such as piperazine (A6), polyamine (A7), and guanido (A8) moieties (Figure 2A). Boc protection is applied to species containing multiple amines to enhance selectivity (Figure S6). The primary amines also cleave trithiocarbonate end-groups, so hydroxyethyl acrylate is used as a capping agent.

A notable advantage of employing poly(pentafluorophenol acrylate) is the ability to assess the extent of amidation via ^{19}F NMR (Figure S5). Complete conversion is confirmed by the disappearance of poly(pentafluorophenol acrylate) peaks. The number-average molecular weight (M_n) and $f_{hydrophilic}$ are calculated assuming a poly(n-butyl acrylate)$_{118}$-*b*-poly(cationic)$_{100/150/200}$ block composition (Figures S3 and S7–S16). Finally, potentiometric titrations on the amphiphiles show that pK_a values range from 7.2 to 8.3, with the A7 modification exhibiting two pK_as at 5.6 and 8.2 (Table S1). This postpolymerization modification approach provides a robust framework for systematically varying polymer scaffold properties, allowing for precise control over corona cation density and hydrophilic–hydrophobic balance.

The self-assembly of polycationic amphiphiles to form micelles is performed via an ultrasound-assisted direct dissolution technique. Dry powders of the amphiphiles are directly dissolved in MOPS buffer at pH 7 via stirring at room temperature for 3 days with 30 min of ultrasonication every 24 h. Dynamic light scattering (DLS) is used to assess the size distribution, revealing intensity-weighted mean diameters (Z-Average value) ranging from 70 to 130 nm, displaying a narrow monomodal distribution for the entire polymer library (Figure 2D). While variations in the hydrophilic block length did not produce a linear change in micelle size, the amine identity is found to influence micelle size trends. Specifically, an increase in the amine hydrophobicity was positively correlated with larger micelle sizes. Furthermore, the direct dissolution micelle assembly method typically results in the formation of non-ergodic micelles, where polymer characteristics and preparation techniques significantly influence size.[54] Given the consistent synthesis and formulation methodology applied across the library, these size trends are inherent characteristics that play a critical role in dictating the reproducible properties of polybasic amphiphiles.

Chemical Features Affect mRNA Binding and MNP Size/Stability

The efficacy of mRNA delivery vectors hinges on both efficient complexation and the release of the bioactive cargo. The influence of amphiphile identity on micelle–mRNA binding and release dynamics is assayed via two modified versions of a RiboGreen-based dye exclusion assay (Figure 3A). The assays simulate changes in micelleplex stability in cell culture media and mRNA release and are conducted at N/P (molar ratio of micelle nitrogen (N) content to mRNA phosphate (P) content) ratios of 5 and 10. The first assay demonstrates a high degree of complexation (~98%) of all micelles in PBS buffer at both N/P ratios with no clear trends (Figure 3B). However, high binding efficiency does not necessarily indicate stable micelleplexes. To elucidate micelleplex behavior in complex cell culture media, micelleplex formulations (post-RiboGreen assay) are subject to dilution in cell culture media (OptiMEM). Changes in micelleplex stability result in mRNA expulsion, increasing RiboGreen fluorescence. Across the micelle library, N/P 5 formulations exhibit a comparative increase in fluorescence (indicative of decreased relative binding efficiency) over N/P 10 formulations. This indicates more mRNA release from low N/P formulations, implying a decrease in MNP stability. This suggests that MNP formation at a higher N/P of 10 is more stable in culture media (Figures 3B and S18).

To gauge the relative binding strength of MNPs, we used a modified dye exclusion assay with the addition of heparan sulfate (Figures 3B and S18), an anionic sulfonate glycosaminoglycan ubiquitous on cell surfaces and known to cause nucleic acid release from delivery vehicles. Pearson pairwise correlation values assess relationships between input features of amine chemistry, corona length, and relative binding strength values (from RiboGreen fluorescence increase upon heparan sulfate incubation) (Figure S19). Results show that greater amine substitution and hydrophobicity lead to a weaker relative mRNA binding strength and more release. mRNA release increases linearly across A1–A5 due to increasingly bulky and hydrophobic substitutions on the amines. Notably, A7 and A8 MNPs exhibit low mRNA release, indicating very stable and compact formulations. MNPs displaying hydroxyl groups (A9 and A10), had similar stability to their nonhydroxylated counterparts (A1 and A2), potentially due to additional hydrogen bonding interactions with mRNA, negating the effect of bulky substitutions. These findings show that less substituted amines improve mRNA-micelle binding and underscore the chemistry in optimizing micelleplex stability and mRNA release, which is crucial for enhancing delivery efficiency and therapeutic efficacy.

Micelleplex size is another key parameter that impacts cellular internalization and the functional delivery of mRNA. DLS measurements show that the MNP hydrodynamic size distribution generally ranges between ~150 nm to ~250 nm in PBS at both N/P ratios of 5 and 10 (Figure 3C and Tables S2 and S3). N/P 10 formulations generally offer smaller MNPs in PBS (ca. 100–200 nm) than in N/P 5, suggesting higher mRNA compaction. In contrast, the increased particle size at a lower N/P ratio is likely due to micelle aggregation, potentially forming dimers or trimers during mRNA complexation. This phenomenon is likely driven by intermicellar interactions facilitated by partial charge neutralization at lower N/P ratios, leading to reduced electrostatic repulsion and increased clustering. A correlation is found with amine hydrophobicity wherein more hydrophobic amines result in larger aggregates. However, MNPs displaying A8 emerge as an exception that form large aggregates at N/P 5. OptiMEM addition, however, results in some degree of MNP aggregation evident from an increase in hydrodynamic diameter, likely due to counterion-induced aggregation ranging into microns. Again, MNPs bearing bulky hydrophobic amines (A5, A5, and A6) show a higher level of aggregation evident from an increase in MNP hydrodynamic diameter. These findings show that both the MNP formulation ratio and the amine hydrophilicity and side-chain bulkiness affect MNP stability, an important feature for optimizing mRNA delivery systems.

Amine Identity Dictates MNP Delivery Performance *In Vitro*

To elucidate the impact of physicochemical structure on mRNA delivery efficacy, micellar nanoparticles (MNPs) were formulated using mRNA encoding green fluorescent protein (GFP). Delivery experiments were conducted across a range of therapeutically relevant cell lines, including HEK293T (kidney), A549 (lung), HuH7 (liver), and HDFn (fibroblasts), yielding promising results (Figures 4B,C and S22–S27). The efficacy of mRNA delivery was evaluated using flow cytometry, which provided two key metrics: the percentage of GFP-positive cells (indicating delivery efficiency) and the mean fluorescence intensity (MFI), which reflects the extent of GFP expression within individual cells. In delivery experiments with HEK293T cells, all MNP formulations were tested across different N/P ratios and mRNA dosages.

The GFP expression levels of MNP formulations in HEK293T cells at N/P ratios of 5 and 10, across three different

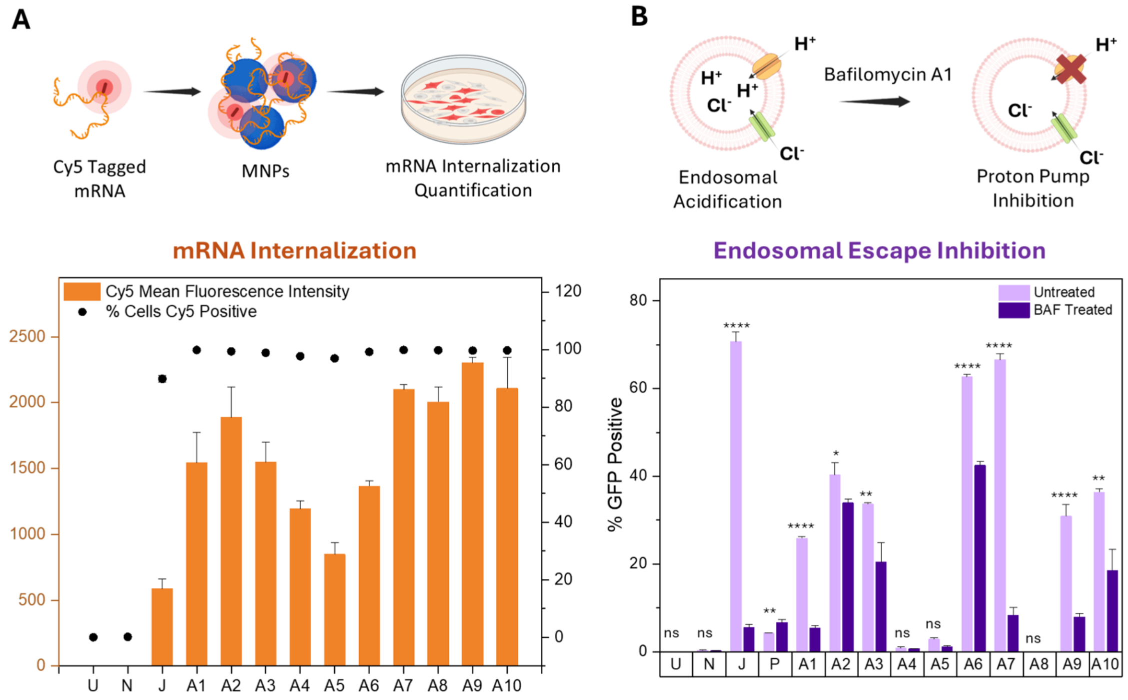

Figure 5. (A) Graphical representation of percentage of cells positive for Cy5 fluorescence indication successful internalization of mRNA-loaded micelleplex and respective Cy5 MFI to quantify the relative amount of Cy5-labeled mRNA internalized ($t = 24$ h). U = Untreated, N = Naked mRNA, J = JetPEI. (B) HEK293T cells are preincubated with Bafilomycin-A1, which is a proton pump inhibitor. Reduction in GFP-positive cells upon BAF treatment indicates a reliance of micelleplexes on endosomal acidification to escape the endosome. Poly-L-lysine (P) was used as a negative control and JetPEI as a positive control. Student's unpaired *t* test was used to determine statistical significance.

mRNA dosages (Figures 4B,C and S22−S24), demonstrate a positive correlation between N/P ratio, mRNA dosage, and GFP expression levels. This correlation is attributed to the interplay between nucleic acid compaction and the ability of excess cationic polymers to facilitate endosomal escape mechanisms. Notably, significant variations in the delivery performance are closely linked to the identity of the amine components within the MNP corona. Preliminary data analysis reveals a consistent trend: increased amine bulkiness correlates with decreased delivery efficiency and GFP MFI. Notably, although A3 MNPs achieve high delivery efficiencies, their corresponding GFP MFI is significantly lower compared to those of A1 and A2 variants. Similarly, A6 MNPs, which contain a piperazine-based amine moiety with bulky substitutions, exhibit a notably lower GFP MFI, suggesting suboptimal performance due to premature mRNA release and poor delivery. In contrast, hydroxyl modifications of primary and secondary amine-based pendant groups (A9 and A10) lead to higher GFP MFI compared to their nonhydroxylated counterparts (A1 and A2), indicating that such modifications may enhance mRNA delivery and release. The A7 MNPs are the top-performing formulations even at lower N/P ratios. The dual pK_a exhibited by A7 (Table S1) likely increases endosomal escape and mRNA release and translation.[55] The guanido-based A8 MNP exhibited unexpected poor performance despite the known activity of guanidine chemistry leading to cell permeation and pDNA-based gene expression.[34,56] We hypothesize that A8 MNPs, due to their guanidinium groups, introduce additional hydrogen bonding interactions with mRNA, leading to stronger binding and significantly altering mRNA complexation-decomplexation dynamics. Importantly, these observed trends, although detailed for HEK293T cells, were also consistent across the other cell lines studied (Figure S27).

The relationship between the physicochemical parameters and delivery was quantitatively analyzed by SHAP TreeExplainer analysis.[57] SHAP is a game theoretic approach employed to extract the importance of a given model variable (polymer features) on a predicted output (delivery performance) based on initial learning data. Key polymer-dependent features such as side-chain molecular volume (bulkiness) and $c \log P$, relative binding efficiency, pK_a, micelle size, and MNP size were considered as independent input variables (Figures 4D,E and S39). Different machine learning (ML) models were trained on distinct subsets of data derived from 3780 experimental measurements. These subsets were carefully selected to evaluate how different input features influence various biological outputs (see the Materials and Methods section for details). To validate the robustness of our ML model results, we conducted 5-fold cross-validation and have reported test R^2 values in the prediction of different properties in Table S5. SHAP analysis of the *in vitro* data highlights that MNP size is the most critical determinant of delivery efficiency and GFP mean fluorescence intensity (MFI), as illustrated in the radar plots (Figure S39D−F). Although amine hydrophobicity and bulkiness influence mRNA binding capacity to MNPs, thereby affecting delivery outcomes, these features are less directly perceived by cells compared with the physical attribute of particle size. Interfeature dependencies, depicted through Pearson correlations (Figure S19), show that MNP size is positively correlated with side-chain hydrophobicity, a relationship emphasized in the SHAP dependency plots (Figure S40). The pronounced impact of MNP size arises from the formation of larger, less compact structures due to hydrophobic and bulky amine substitutions.

Additionally, SHAP plots demonstrate a strong influence of mRNA binding efficiency on both delivery efficiency and GFP MFI. This is evident in Figure 4F,G, where delivery efficiency

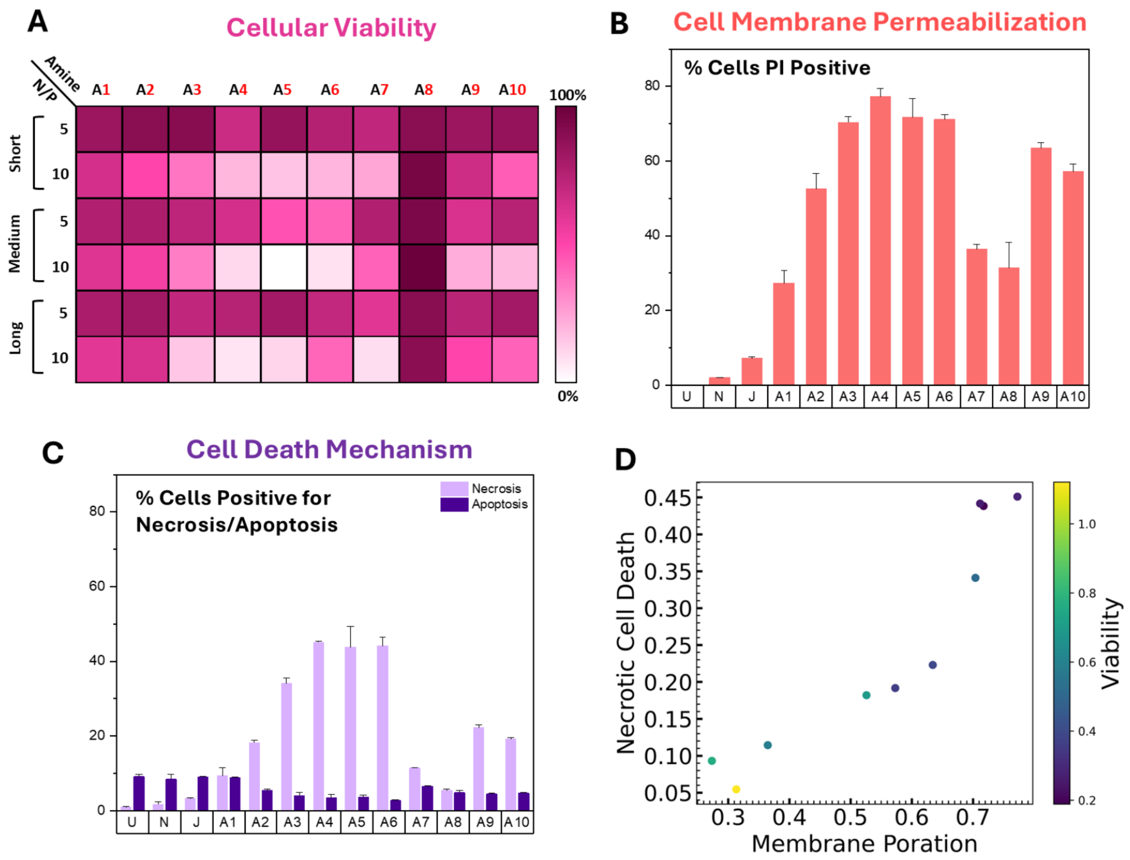

Figure 6. (A) Heatmap showcasing the cellular viability of HEK293T cells upon transfection with the full micelle library (obtained via CCK-8 Assay). (B) Percentage of cell positive for propidium iodide (PI) indicates the degree of membrane permeabilization by the MNPs. (C) Percentage of cells positive for necrosis and/or apoptosis upon treatment with the respective MNPs. (D) Correlation between viability, membrane permeabilization, and necrotic cell death. Higher membrane permeabilization leads to increased necrosis contributing to decreased viability.

increases linearly with increasing binding efficiency, while GFP MFI peaks at intermediate binding values. This suggests that stronger mRNA binding enhances the stability and delivery efficiency by minimizing premature decomplexation before cellular entry. Conversely, an optimal intermediate binding strength ensures efficient cytosolic release, resulting in higher GFP expression. Notably, the analysis also indicates a negligible role of corona length (Figure 4D,E) in dictating biological outcomes, supporting our initial experimental observations that the length of the cationic micelle corona does not significantly impact delivery, likely due to its inherently high cation density. Overall, these data highlight the crucial role of physicochemical characteristics in optimizing mRNA delivery via micellar nanoparticles, demonstrating how parameters such as MNP size, amine bulkiness, and mRNA binding efficiency directly influence delivery efficiency and GFP expression.

Amine Identity Dictates MNP Uptake and Endosomal Escape to Enhance mRNA Delivery

We next sought to correlate the mechanistic impetus regulating delivery performance to the polymer features to create a holistic design blueprint. Since the corona length of MNPs did not significantly affect their delivery performance, formulations with a medium-length corona complexed with GFP mRNA were selected for more detailed mechanistic investigations. Delivery experiments using Cy5-labeled GFP mRNA indicated over 90% internalization across all 10 micelles at the 4 h mark, a trend that persisted even at 24 and 48 h (Figures 5A and S28). To assess relative cellular internalization, we measured the geometric mean fluorescence intensity (MFI) of Cy5. Notably, when comparing the Cy5 MFI at 24 h with amine identity, we observed that micelles with poorer binding affinities resulted in reduced internalization of mRNA payloads. Furthermore, the internalization of nanosystems can occur through various endocytic and macropinocytotic pathways.[58−60] To probe internalization mechanism, cells were co-incubated with MNPs containing Cy5 mRNA and specific drugs known to inhibit certain internalization pathways.[61] The results showed that all MNP formulations primarily relied on clathrin-mediated endocytosis, with some contributions from caveolar endocytosis and macropinocytosis (Figure S29). While amine identity does not seem to impact the preferred uptake pathway, the dependence on clathrin-mediated endocytosis, an endolysosomal pathway, indicates a downstream dependence of the observed delivery performance on endosomal escape propensity.

Upon entering the endolysosomal pathway, micelleplexes encounter two potential outcomes: successful translocation to the early endosome with subsequent cytoplasmic release, or entrapment in the late endosome, leading to lysosomal degradation.[62] The latter scenario, driven by V-ATPase proton pumps, presents a primary bottleneck in nucleic acid delivery. Amine-based polycations with pK_a values ≤6 exhibit buffering capacity, acting as “proton sponges” during endosomal acidification.[63,64] This buffering induces chloride counterion influx, causing endosomal swelling, membrane destabilization, and rupture. Additionally, protonation of micelleplexes during

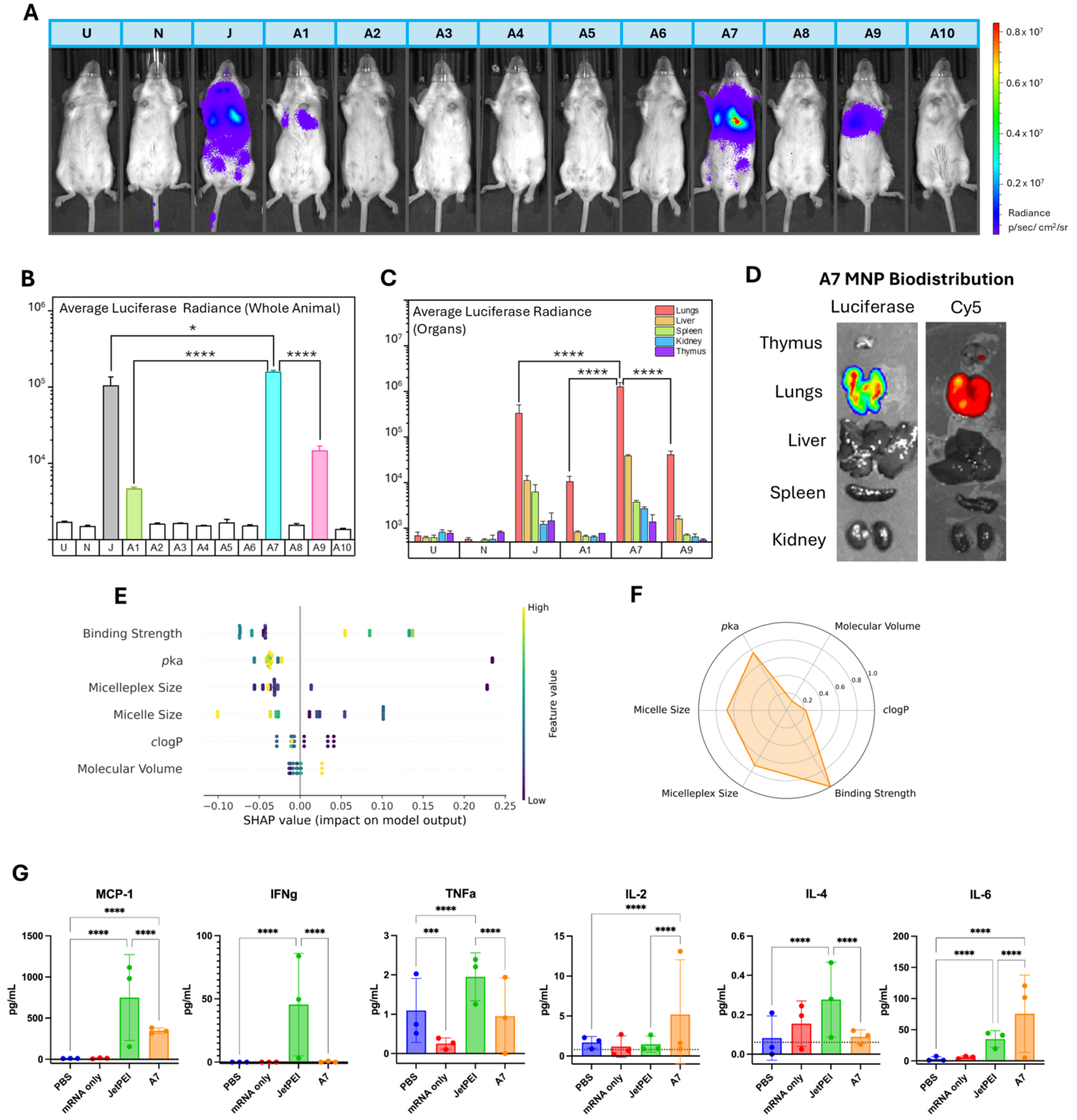

Figure 7. (A) *In vivo* luminescence images obtained via an IVIS imager for Fluc mRNA delivery with Md library MNPs via IV tail vein injection. Single images are shown for representation. Experiments were performed in triplicate ($n = 3$). (B) Average luciferase radiance for the whole animal ($n = 3$). (C) Average luciferase radiance for organs. (D) Luciferase luminescence and Cy5-tagged mRNA biodistribution are highly localized in the lungs for the A7 MNPs. (E) SHAP analysis representing polymer feature dependencies of *in vivo* luciferase activity. (F) Radar plot representing the average SHAP values of input parameters corresponding to the biological output (*in vivo* luciferase activity). (G) Plasma cytokine levels 6 h postinjection of MCP-1, IFNg, TNFa, IL-2, IL-4, IL-6. Data points represent an average of 2 technical replicates for $n = 3$ animals per group. The horizontal dotted line represents lower limit of quantification. Any values plotted below this line are extrapolated from the standard curve. Two-way ANOVA and Šídák's multiple comparisons test with $\alpha = 0.05$ were used to identify statistically significant differences between groups. U = Untreated, N = Naked mRNA, J = JetPEI.

buffering may release micelles to maintain charge balance, which can interact with and disrupt the endosomal lipid bilayer, forming pores and facilitating escape.[63] Bafilomycin-A1 (Baf-A1), an H^+-ATPase inhibitor was added to cultures to block proton influx into cellular endosomes (preventing proton sponge-mediated escape).[65,66] A significant decrease in GFP expression level upon Baf-A1 treatment is found across MNPs, indicating a primary reliance on proton sponge-mediated endosomal escape (Figure 5B). The pendant amine groups of A7 typically share a proton at higher pH levels, becoming individually protonated as the pH decreases resulting in the dual pK_a observed.[55] Consequently, A7 displays a broad buffering region, indicating superior buffering capacity and resulting in the largest drop in GFP expression (∼90%). MNPs displaying A1 and A9 also yield a substantial decrease (∼75%) in GFP expression, while A3, A6, and A10 exhibit an intermediate decrease in GFP expression levels (∼40%). Overall, micelles with lower pK_a values enhance endosomal escape (Figure S30).

Overall, we observed a robust link between the identity of amine groups and mechanistic attributes of observed biological performance. These data demonstrate that while all micelle formulations ensured high levels of mRNA internalization, the efficiency is dictated by the binding affinity. Moreover, the reliance on the "proton sponge" effect of amines with specific pK_a values significantly influenced endosomal escape, highlighting the importance of amine titratability in the design of effective gene delivery systems.

Amine Identity Dictates MNP Toxicity and Cellular Viability *In Vitro*

Toxicity assays allow fundamental insights into how chemical parameters, such as amine substitution and hydrophilicity, affect cellular viability, which is crucial for the rational design of polymer-based systems. CCK-8 assays measure the metabolic activity of cells and offer a first-pass measure of delivery system toxicity (Figures 6A and S22−S24). The cell viability profiles of individual micelles show a negative correlation with an increasing micelleplex N/P ratio and mRNA dosage. While higher N/P ratios and mRNA dosage improve delivery efficiency due to the surplus cations, this effect is counterbalanced by a reduction in cell viability, likely due to the necrotic effects of excessive cationic functionalities. The identity of the amine substitution also has a discernible effect on the viability profiles. Amines bearing hydrophobic and bulky substitutions correlate with a decline in transfection efficiency, particularly evident when comparing variants A1 through A5. The viability trends linearly decrease from A1 through A5, with A5 displaying high necrotic cell death. Similarly, high levels of cell death are seen for the piperazine-based A6 micelles. Hydroxyl modification of primary and secondary amine-based groups (A9 and A10) negatively affects viability in comparison to nonhydroxylated counterparts (A1 and A2). In contrast, A7 micelleplexes display moderate viability, while A8 micelleplexes do not elicit cytotoxicity, despite effective internalization. Again, we did not observe any correlation between micelle corona size and *in vitro* viability, which is further demonstrated via SHAP analysis (Figure S39C). While these observations are for HEK293T cells, the same amine-dependent trends are observed across the other cell lines as well (Figure S27).

Given that cationic nanoparticles are known to induce membrane porosity, we examined the impact of membrane destabilization on cell viability. Propidium iodide (PI), a dye that enters cells with compromised membranes, is used to assess this destabilization. Greater substitution on amines results in a greater PI signal, indicating membrane permeation (Figure 6B). Both excessive hydrophobicity and hydrophilicity amplify this effect, with hydroxyl-modified amines (A9 and A10) showing PI internalization levels comparable to their more hydrophobic counterparts (A4 and A5). Performing PI internalization assay in tandem with Annexin V assay delineates subpopulations undergoing apoptosis or necrosis[67,68] (Figure 6C). Annexin V binds to phosphatidylserine exposed on the cell surface during death, indicating necrosis if accompanied by PI positivity (due to membrane poration) or apoptosis if Annexin V is positive alone (Figure S20). The correlation between necrosis levels and membrane destabilization, as assessed by PI internalization, is significant (Figure 6C,D). Apoptosis levels remain consistent across the treatment library, suggesting that while some degree of membrane permeabilization is crucial for effective transfection and endosomal escape, excessive destabilization can lead to an increase in necrosis, compromising cell viability. Overall, micelles with more hydrophobic and bulky pendant amine groups (A4−A6) cause an increase in necrosis, indicating their potential unsuitability (Figure 6D). Interestingly, micelles such as A1, A2, and A7, which cause only intermediate reductions in cell viability, exhibit low necrosis levels, suggesting that a reduction in cell viability may be due to a slowdown in cell growth rather than necrotic death, highlighting the importance of selecting amine modifications that balance efficacy with minimal cytotoxicity.

Amine Identity Dictates *In Vivo* Delivery Performance

To evaluate the *in vivo* delivery performance of MNPs, we bound luciferase-encoding mRNA to the MNP formulations. These MNPs were administered by tail vein injection to immune-competent BALB/c mice to quantify luciferase expression through live-animal luminescence imaging (Figures 7A and S32). The animals were sacrificed 6 h postinjection, and organs were harvested to measure organ luminescence, which serves to assess biodistribution. Below, we focus on data from MNPs with the medium cation corona length (at N/P 10 and mRNA dosage of 0.5 mg/kg), given the absence of significant performance differences among MNPs A7 short, medium, and long in *in vivo* delivery screens (Figure S33) and the consistent data from the entire MNP library in cell culture models (Figure 4B,D). Collectively, these results highlight the critical influence of amine identity on delivery efficiency.

Intravenous administration of the medium library MNP displaying cations A1−A10 demonstrates disparate *in vivo* performance, with only A1, A7, and A9 micelles exhibiting significant luciferase signal indicative of successful luciferase expression (Figure 7A,B). The luminescence signal for these MNPs is predominantly localized in the thoracic region. MNP A7 displays the highest luminescence at 3×10^6 p/s/cm^2/sr, comparable to that of the commercial control *in vivo*-JetPEI and an order of magnitude greater than A1 and A9 MNP formulations at the same dosage. Organ-level luciferase signaling revealed lung-specific biodistribution of the luminescence for all three MNP identities (Figure 7C). A7 MNPs displayed lung luminescence (1.2×10^7 p/s/cm^2/sr) significantly higher than that of *in vivo*-JetPEI (3.9×10^6 p/s/cm^2/sr), indicating delivery specificity. This was further validated by the delivery of Cy5-labeled mRNA and organ imaging, which confirmed that A7 MNPs predominantly localized in the lungs (Figure 7D). The ability of A7 MNPs to achieve highly selective lung accumulation and expression is particularly significant, as it contrasts with existing organ-selective LNP formulations, which while capable of lung-specific mRNA translation, still exhibit substantial hepatic accumulation. We attribute this enhanced specificity to the homogeneous single-component nature of our MNPs, in contrast to the multicomponent lipid-based LNPs, which have been shown to accumulate in the liver due to the presence of cholesterol and phospholipids.[69] These findings show the ability of the A7 MNPs to circumvent hepatic sequestration without requiring extensive formulation optimization, thus, highlighting its potential as a highly efficient and

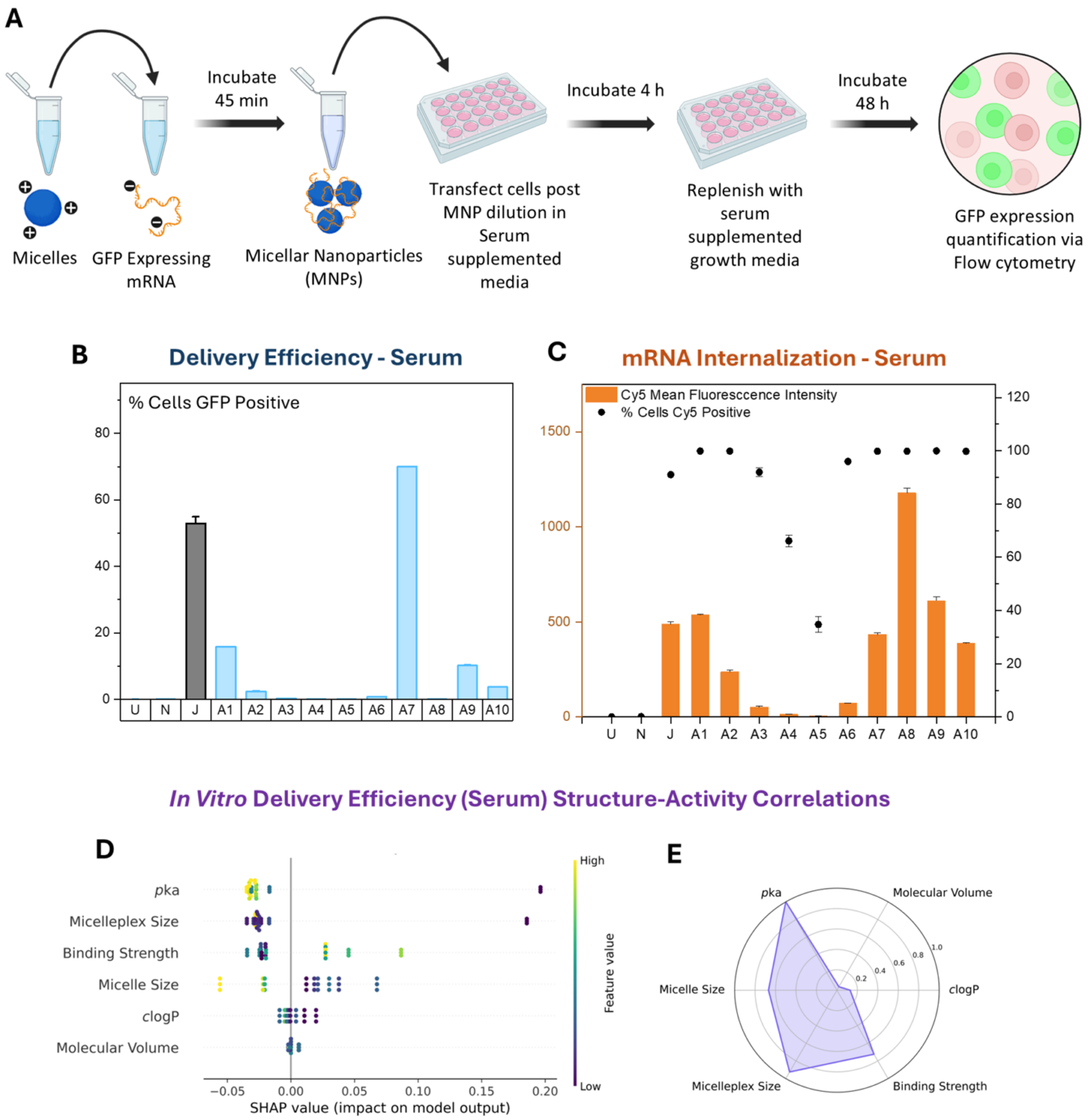

Figure 8. (A) Scheme for *in vitro* transfection in the presence of serum. (B) Percentage of HEK293T cells reported as GFP-positive via flow cytometry for Md library series of micelles transfection at N/P 10 and 0.5 μg mRNA/well dosage (t = 48 h) in the presence of serum (DMEM + 10% FBS). (C) Percentage of cells positive for Cy5 fluorescence and respective Cy5 MFI for Md series of micelle transfection in the presence of serum (DMEM + 10% FBS) (t = 24 h). U = Untreated, N = Naked mRNA, J = JetPEI. (D) SHAP analysis representing polymer feature dependencies of *in vitro* transfection efficiency in the presence of serum. (E) Radar plot representing the average SHAP values of input parameters corresponding to the biological output (transfection efficiency, serum present).

simplified platform for pulmonary mRNA delivery. SHAP analysis further revealed that the relative binding strength between micelles and mRNA is the dominant factor influencing luciferase activity, followed by pK_a and MNP size (Figure 7E). This trend reinforces the critical role of binding strength in ensuring the stability of cargo against serum protein-induced decomplexation yet enabling effective cytoplasmic release. It also explains why A10 MNPs, despite performing on par with A7 *in vitro*, failed *in vivo*. A10's weaker binding affinity relative to A7, which facilitated greater mRNA release and higher GFP MFI *in vitro*, likely caused premature decomplexation during circulation, ultimately compromising mRNA delivery. The emergence of pK_a as an influential parameter is notable, as previous research has established its role in determining organ specificity. Nanoparticles with high pK_a (>8), particularly those containing nitrogenous moieties, are enriched with proteins having a pI (isoelectronic point) below physiological pH in their nanoparticle corona.[41] These nitrogenous groups, such as quaternary ammonium species, facilitate the adsorption of vitronectin, which aids in binding with $\alpha v\beta 3$ integrin receptors on the endothelial cells within lung capillaries, ultimately directing tissue-specific delivery.[41,44] Since A1, A7, and A9 micelles display a corona pK_a of around 8, we attribute a similar mechanism to account for the MNP targeting to the lungs to that previous study.[41] However, further investigation of the cationic MNP's lung specificity is ongoing to clarify the exact mechanisms.

Injected mice displayed no discernible adverse events following MNP administration. *In vivo* tolerability assessments of A1, A7, and A9 MNPs at N/P 10 with an mRNA dosage of 0.6 mg/kg revealed no significant alterations in ALT, AST, BUN, or creatinine serum levels compared to untreated controls 24 h postadministration, indicating unaffected renal and hepatic functionality (Figure S35). To further probe the potential for MNP-induced tissue damage and an inflammatory response, cytokine profiling was conducted. We collected plasma samples 6 h postinjection for analysis of pro-inflammatory cytokines including MCP-1, IFNγ, TNFα, GM-CSF, IL-1β, IL-2, IL-4, IL-6, IL-10, and IL-12p70 (Figures 7G and S38). Notably, JetPEI triggered marked elevations in MCP-1, IFNγ, TNFα, and IL-4, relative to the PBS-injected controls, while the A7 MNP group exhibited a moderate MCP-1 increase, significantly lower than that of JetPEI but above control levels. Crucially, no significant upregulation of IFNγ, TNFα, or IL-4 was observed in the A7 cohort. Histopathological evaluation via hematoxylin and eosin staining revealed no differences in gross pathology across lung and liver tissues between the groups (Figures S36 and S37). Although modest inflammatory signatures and minor histological changes were detected, these are congruent with the delivery methodology employed. Elevated cytokines, particularly in the *in vivo*-JetPEI and A7 groups, are predominantly linked to monocyte and macrophage activation, which are abundant in pulmonary tissues.[70] The heightened levels of IL-6 observed in the A7 group likely result from membrane permeabilization, triggering the release of damage-associated molecular patterns (DAMPs). These DAMPs, in turn, activate pattern recognition receptors (PRRs) on macrophages, initiating IL-6-mediated acute-phase inflammatory cascades.[71] The preferential lung tropism exhibited by A7 MNPs likely produces the greatest membrane disruption. In contrast, the reduced delivery efficacy of A1 and A9 in pulmonary tissues correlated with diminished IL-6 induction, indicative of less tissue perturbation (Figure S35). *In vivo*-JetPEI, despite its lung specificity, induced lower IL-6 levels than A7, likely due to its reduced membrane-permeabilizing capabilities. Collectively, these data highlight the favorable tolerability and robust lung-targeting capacity of MNP formulations for mRNA delivery. Looking forward, such precision in pulmonary nucleic acid delivery holds significant potential for advancing next-generation therapeutic interventions targeting chronic conditions including cystic fibrosis and acute respiratory distress syndrome (ARDS).

In Vitro MNP Delivery Performance in the Presence of Serum Serves as a Predictor of *In Vivo* MNP Delivery Success

Serum proteins are known to adversely affect polyplex compaction, leading to premature unpackaging of genetic payloads and hindering payload internalization.[38,39] We hypothesized that serum protein fouling might explain the disparities observed between *in vitro* and *in vivo* mRNA delivery performance, prompting us to examine their impact on the MNP system under *in vitro* conditions. To investigate the role of amines in resisting serum fouling, we conducted *in vitro* transfection assays in HEK293T cells, using culture media supplemented with 10% fetal bovine serum instead of OptiMEM (Figure 8A). Flow cytometry analysis revealed that GFP expression levels for the A7 MNP were high and comparable to those observed under serum-reduced conditions. In contrast, formulations containing A1 and A9 exhibited slightly lower expression, while A2 and A10 demonstrated poor performance, achieving less than 5% expression (Figures 8B and S31A). Additionally, cellular viability was markedly improved across all formulations (Figure S31B)

SHAP analysis revealed that pK_a and MNP size are the most significant factors influencing delivery efficiency under serum conditions, with binding efficiency ranking third (Figure 8D). The high binding efficiencies of A1, A7, and A9, attributed to their primary amine content, likely contribute to stable micelleplexes (lower mRNA decomplexation) in the presence of serum proteins, thereby enhancing the delivery performance. This is further corroborated by Cy5-labeled mRNA uptake assays, which demonstrate that micelles with strong binding capabilities promote greater overall mRNA internalization in serum (Figures 8C and S31C,D).

The superior performance of A7 under both *in vivo* and *in vitro* (under serum) conditions, alongside the considerable activity of A1 and A9, suggests a correlation between *in vitro* (under serum) and *in vivo* delivery. To explore this, we applied multitask Gaussian Process (GP) models, using BoTorch[72] to evaluate the predictive value of *in vitro* data for *in vivo* activity, incorporating data from both serum-supplemented and OptiMEM conditions (Figure S41). Input data were scaled using min-max normalization, while outputs were standardized with z-score normalization to prepare for multitask GP training. The multitask GP model, trained on both *in vitro* and *in vivo* data sets, enabled us to examine correlations across tasks. To assess the robustness of our predictive framework, we further trained the model on five different subsets of training data (Table S6). Results showed that incorporating *in vitro* (serum present) data improved predictions for *in vivo* activity more effectively than incorporating *in vitro* (serum reduced) data. This enhancement was quantitatively supported by the task covariance matrix from the GP model, with a covariance of 0.935 ± 0.05 between *in vitro* (serum present) and *in vivo* activity, significantly higher than the covariance between *in vitro* (serum reduced) and *in vivo* activity (0.342 ± 0.09) (Table S6). This finding highlights the serum-based *in vitro* data as more representative of the biological processes critical for predicting *in vivo* performance. Additionally, true vs predicted plots validated that multitask models, especially with serum-based data, substantially improved predictions of amine-mediated trends *in vivo*.

This comprehensive analysis provides a nuanced understanding of how key polymer features influence mRNA delivery performance both *in vitro* and *in vivo*, revealing complex relationships among these variables. While structure−activity relationships observed in serum-free *in vitro* delivery diverged notably from *in vivo* outcomes, delivery in the presence of serum *in vitro* appears to better predict *in vivo* success. These findings support the idea that the integration of serum conditions in *in vitro* screens can serve as a rapid and inexpensive qualitative model for signaling the possibility of *in vivo* delivery success, accelerating the development of targeted, stable, and effective nanoparticle systems for gene therapy applications.

■ CONCLUSIONS

In conclusion, this study presents an innovative approach for generating a diverse library of polycationic diblock amphiphiles, aiming to rapidly develop micelles for efficient mRNA delivery in both *in vitro* and *in vivo* settings. Utilizing a postpolymerization functionalization strategy, a library of amphiphiles containing three molecular weights and 10 distinct amine moieties are assembled into micelles. *In vitro* delivery studies using a reporter gene assay demonstrate that micelles with stronger mRNA binding capabilities (A1 and A7) transfect more cells, whereas those with intermediate binding tendencies deliver a higher amount of functional mRNA per cell (A2 and A10). This indicates that balancing the binding strength is likely crucial to achieving optimal delivery performance. Moreover, micelles with hydrophobic and bulky pendant groups (A3, A4, and A5) tend to induce necrosis during cellular delivery, leading to a reduction in cell viability. Further cellular uptake studies, examining internalization mechanisms and endosomal escape efficiency, revealed that micelles with enhanced buffering capacity both improve endosomal escape and increase mRNA internalization, boosting the delivery efficiency. Among the synthesized amphiphiles, a polyamine-based pendant moiety, labeled A7, emerged as the most effective, showcasing exceptional delivery results across multiple cell lines. This superior performance is also shown *in vivo*, where A7 selectively targets the lung and results across the library align with serum-present *in vitro* delivery trends. To gain a deeper understanding of the correlation between amine structure and biological performance, SHAP analysis was applied. This analysis confirmed that binding efficiency plays a pivotal role in determining delivery potential while also identifying micelle nanoparticle (MNP) size as a critical factor in delivery efficacy. Multitask Gaussian Process models further established a strong correlation between *in vitro* performance in the presence of serum and *in vivo* outcomes, offering valuable insights for the design of future micelle-based mRNA delivery systems. Overall, this study sets a new benchmark for mRNA delivery technologies by addressing key challenges, such as delivery efficiency, cytotoxicity, and organ targeting, while integrating experimental and machine learning insights to offer a new paradigm for designing micelle-based systems with enhanced precision and efficacy. This work establishes a promising and robust framework that could accelerate the development of next-generation therapeutics in gene therapy, laying the foundation for groundbreaking advancements in nanomedicine.

■ MATERIALS AND METHODS

Synthesis of Poly(nBA)-*b*-poly(PFPA) Diblock Polymer Scaffold

All chemicals were purchased from Sigma-Aldrich and used without further purification. Pentafluorophenol acrylate was synthesized as outlined in the Supporting Information. Poly(nBA)-DDMAT macro-CTA was synthesized by the bulk RAFT polymerization of *n*-butyl acrylate (nBA) with 2-(dodecylthiocarbonothioylthio)-2-methylpropionic acid (DDMAT) CTA. Following purification and characterization, poly(nBA)-DDMAT macroCTA (1 eq) was weighed into a 10 mL scintillation vial, and pentafluorophenyl acrylate (150, 200, 250 equiv) was added to it. The mixture was then dissolved in 1,4 dioxane (2 M final concentration) to obtain a yellow homogeneous solution. AIBN (0.05 equiv) was added to the mixture, and the vial was degassed via sparging with N_2 (g) for 1 h. The reaction mixture was then stirred at 70 °C for 18 h under a N_2 (g) atmosphere. The reaction was quenched by immersing the flask in liquid nitrogen and opening it to air simultaneously. 70% monomer conversion was estimated from the relative integrations of the signals at −157.78 ppm (1F, polymer) and −157.94 (1F, residual monomer) in the ^{19}F NMR. The reaction mixture was precipitated in ice-cold methanol and dried overnight under vacuum, to obtain the diblock scaffold as an off-yellow powder. Block polymer composition of poly(nBA)$_{118}$-*b*-poly(PFPA)$_m$ was estimated from the relative integrations of the signals at 4.04 ppm(2H, poly(nBA) block), 3.08 ppm(1H, poly(PFPA) block), and 0.94 ppm(3H, poly(nBA) block) in the ^{1}H NMR spectrum of the purified diblock polymer in $CDCl_3$. Finally, given the inevitable variation in molecular weights postmodification, we calculated $f_{\text{hydrophilic}}$ based on repeat units to ensure consistency in our analyses.

Synthesis of Poly(nBA)-*b*-poly(cationic acrylamide) Amphiphilic Diblock Polymers

All 10 polymers for each library (Sh, Md, Lg) were synthesized, in parallel, following a similar generalized procedure: 200 mg of the poly(nBA)-*b*-poly(PFPA) diblock polymer scaffold was weighed into individual scintillation vials. 5 mL of anhydrous DMF solvent was added to each vial and the resultant mixture was stirred until a homogeneous solution was obtained. 20 equiv of hydroxyethyl acrylate were added to the resulting solutions as a capping agent. 2*n* equiv of each amine, where n is the number of PFPA RU of the corresponding scaffold, were weighed into each vial. The vials were then capped, put under nitrogen, and heated to 40 °C for 18 h while stirring. Following completion of reaction, the mixture was allowed to cool down to room temperature and an aliquot was taken for analysis via ^{19}F NMR. Reaction completion was assessed by a complete disappearance of the ^{19}F polymer signals at −152, −157, and −162 ppm. The crude reaction solutions were then purified via dialysis against methanol using a SnakeSkin dialysis bag (3.5 kDa MWCO) and the polymers were then recovered by drying under vacuum.

For diblock polymers bearing Boc-protected side chains (A1, A2, A6−A10), the polymers were dissolved in trifluoroacetic acid (1 mL of TFA per 100 mg of polymer), and the solution was stirred while open to the air for 4.5 h. The crude reaction mixture was concentrated under vacuum. The residue was dissolved in 5 mL of DMF and dialyzed against deionized water, using a SnakeSkin dialysis bag (3.5 kDa MWCO). The polymers were recovered via lyophilization. Polymers were dissolved in DMF-*d7* and purity was confirmed via ^{1}H NMR spectroscopy.

MNP Formulation and Size Measurement

Micelles were prepared via the direct dissolution method. 10 mg of each amphiphile was weighed into individual clean, dust-free, glass vials. Appropriate amounts of MOPS buffer (pH = 7, concentration = 20 mM, ionic strength 100 mM, adjusted with NaCl) were added to obtain 1 mg/mL polymer dispersions. The dispersions were stirred at room temperature for 3 days. The solutions were sonicated for 30 min at every 24 h interval using an ultrasonic bath. During the sonication process, the temperature of the bath was monitored and never exceeded 30 °C. The micelles were filtered through a 0.22 μm GHP syringe filter, and their size distribution was measured with a Malvern Zetasizer Nano ZS (λ = 633 nm) with a scattering angle of 173° at a temperature of 25 °C.

MNP solutions were prepared by diluting micelle and mRNA components in DNA/RNase-free PBS (pH 7.4) unless otherwise specified. All micelle stocks were diluted to a final concentration of 3 nMol of nitrogen per μL. These stocks were then diluted to the appropriate concentration necessary so that upon mixing (equal volumes) with diluted mRNA solution, the appropriate N/P is achieved. For example, in the case of A7 (Md Library), 5 μL of the polymer stock is necessary for every 0.5 μg of plasmid at an N/P = 10. For example, to make a polyplex sample containing 1.5 μg of plasmid at N/P = 10 for a transfection, 15 μL of polymer stock was diluted in 60 μL of PBS to yield 75 μL of micelle stock. For mRNA at 1 mg/mL concentration, 1.5 μL of mRNA stock was added to 73.5 μL of PBS. To form the MNPs, 75 μL of micelle stock was added to 75 μL of mRNA stock, mixed, and then allowed to incubate at room temperature for 45 min prior to use. PNP formulations for JetPEI were prepared following manufacturer protocol.

The hydrodynamic diameter (D_h) of the thus formed MNPs in PBS was determined via DLS using a DynaPro Plate Reader at a temperature of 25 °C. To determine their size distribution upon dilution in cell culture media, the MNPs were first formed in PBS, and their size distributions were recorded and then diluted (3×) with OptiMEM. The OptiMEM diluted MNPs were incubated further for 2 h prior to DLS measurements. The interval of time between addition of media and sample measurement was kept constant for all samples.

RiboGreen Dye Exclusion Assay

Quant-iT RiboGreen was purchased from Thermo Fisher Scientific for dye exclusion studies. mRNA dilution was prepared by adding the required amount of primary mRNA stock (1 mg/mL) to PBS containing RiboGreen to achieve a final concentration of 0.5% RiboGreen by volume. An equal volume of micelle dilution was added to this mRNA dilution form MNPs in accordance with the previously outlined protocol. mRNA stock containing RiboGreen and PBS containing only RiboGreen were used as controls. The MNP solutions (100 μL) were dispensed into a black flat-bottom 96-well microplate using a multichannel pipettor in triplicate, and the fluorescence end point was measured using a microplate reader equipped with a fluorescence filter cube (λ_{ex} = 485/20 nm, λ_{em} = 528/20 nm). The relative fluorescence of each sample was calculated by subtracting the blank (dye-free sample of the corresponding N/P ratio) and then normalizing the result to the polymer-free sample (N/P = 0). The polyplex solutions in the plate were then diluted 3× with OptiMEM (serum-free), and the fluorescence end points were taken 30 min after dilution. To understand the mRNA release dynamics, 10 μL of heparan sulfate dilution in PBS at 1.875 mg/mL (target S/N 10) was added to each well containing the MNPs (100 μL) and the fluorescence increase was measured as described before. The difference in normalized fluorescence intensity due to the addition of heparin was used to compare the extent of mRNA release from polyplexes in the presence of heparin.

Delivery Reporter Assay

GFP expressing mRNA was delivered *in vitro* in HEK293T, HuH7, A549, and HDFn cells to serve as reporter mRNA for successful delivery. The methods outlined herein are similar for all of the cell lines unless otherwise specified. Cells were plated in 48-well plates at 25000 cells/well density 24 h prior to transfection. MNPs were prepared as outlined before, and then 3× diluted with OptiMEM. The media was aspirated off the wells, and the OptiMEM diluted MNPs were added in triplicates to wells and then put in the incubator for 4 h. For example, 75 μL of A7 micelle stock was added to 75 μL of mRNA stock containing 1.5 μg of mRNA, allowed to incubate at RT for 45 min, and then diluted with 300 μL of OptiMEM to a total volume of 450 μL. This solution was immediately added to wells in triplicate such that each well received 150 μL total containing 0.5 μg mRNA dose. After 4 h of incubation, each well was topped with cell-specific growth media containing 10% FBS. Positive control, jetPEI, was used according to the manufacturer's protocol for transfection at an N/P of 5. 24 h post-transfection, the media on the cells was replaced with fresh supplemented growth media. All transfections were done at N/P of 5 and 10 at mRNA dosages of 0.5 μg/well. A dosage screening was done in HEK293T cells at 0.25, 0.5, and 0.75 μg/well.

48 h post-transfection, the cell viability was assessed by CCK-8 Assay. To prepare the assay solution, an appropriate volume of CCK-8 solution was added to Fluorobrite DMEM (w/10% FBS) to achieve a final dilution of 8% CCK-8 solution. The media was aspirated off from the well, and 500 μL of CCK-8 dilution was added to each well and put in the incubator for 2 h. Post incubation, 100 μL of CCK-8 media in the well was aliquoted into clear-bottom 96-well plates, and the absorbance at 450 nm was measured on a Synergy H1 Hybrid Reader (BioTek; Winooski, VT). The absorbance was normalized to untreated controls to obtain the relative cellular viability for each condition.

Post CCK-8 assay, the media was aspirated off the well, and the cells were trypsinized and then transferred to 2 mL deep-well plates. The cells were washed with PBS, pelleted via centrifugation (1000*g* for 10 min at 4 °C), and then resuspended in PBS containing 2% FBS. The PBS dilution also contained calcein violet AM to enable delineation of live cell populations. For delivery efficiency, the percentage of live cells expressing GFP was measured via flow cytometry on a Bio-Rad (Hercules, CA) ZE5 flow cytometer with the 405 and 488 nm laser channels activated. The data were analyzed with FlowJo software. Gating schemes are represented in Figure S21.

For delivery in the presence of serum, the methodology outlined above was followed with one modification. The MNP formulations were diluted 3× with DMEM containing 10% FBS instead of OptiMEM. The rest of the protocol was kept the same.

For internalization assays, Cy5-labeled GFP expressing mRNA (EZ Cap Cy5 EGFP mRNA (5-moUTP), ApexBio Technology) was used as the reporter gene. The delivery protocol was kept the same as that outlined above. The percentage of live cells positive for Cy5 and Cy5 MFI were measured via flow cytometry on a Bio-Rad (Hercules, CA) ZE5 flow cytometer with 640 nm laser channels activated. Gating schemes are represented in Figure S21. All internalization studies were done at N/P 7.5 and 0.5 μg of mRNA/well dosage.

In Vivo Studies

All animal studies were approved by the Institutional Animal Care and Use Committee (IACUC) at the University of Minnesota. The mice were housed within the University of Minnesota's Research Animal Resource facilities, an AAALAC-accredited program. Specific Pathogen Free female Balb/C mice were purchased from The Jackson Laboratory (Strain #:000651). The animals were dosed at 8 weeks old with either PBS, MNP formulations, or JetPEI carrying 10 μg of luciferase mRNA in a total of 200 μL via tail vein injection. Six hours after injection, delivery was assessed by *in vivo* bioluminescence imaging on the IVIS Spectrum 2 (reference funding). Briefly, animals are intraperitoneally injected with D-luciferin substrate (100 μL total volume, 28 mg kg^{-1}). The animals are then anesthetized with isoflurane and placed in the imager where luminescent signal is measured 5 min after substrate injection. Image acquisition is set to 5 min exposure with fStop = 1 and Binning = 2.

The mice were euthanized by CO_2 inhalation for sample collection. Blood was collected by cardiac stick, allowed to clot for 30 min, and then serum was isolated by centrifugation for biochemical analysis. Organs including the lungs, thymus, liver, spleen, and kidneys, were collected in PBS on ice. D-Luciferin substrate was spiked into the PBS and organs were imaged on the IVIS Spectrum 2 (University of Minnesota Imaging Centers, SCR_020997, NIH grant 1S10OD032261). Bioluminescence data was analyzed using Living Image software (version 4.7.3). Organs were then fixed in Formalin and preserved in 70% EtOH for histology.

Histology was performed by the University of Minnesota Masonic Cancer Center's Comparative Pathology Shared Resource. Hematoxylin and Eosin staining was used to assess tissue structure after the administration of MNPs. Lung samples flash frozen in Tissue Plus O.C.T. compound (Scigen) were stained with antiluciferase antibody (cat#) experimental details, analysis tool, and details. Biochemical analysis was performed by the University of Minnesota Veterinary Medical Center Clinical Pathology Laboratory using a Beckman AU480 Chemistry Analyzer. Serum levels of ALT, AST, BUN, and Creatinine were used to assess liver and kidney function 24 h after administration of MNPs. Ten inflammatory markers (GM-CSF, IFNγ, IL-1b, IL-2, IL-4, IL-6, IL-10, IL-12p70, MCP-1, and TNFα) were assessed with the MCYTOMAG-70K-10 Mouse Cytokine MAGNETIC Kit (MilliporeSigma) on a Luminex 200 instrument (Thermo Fisher Scientific).

Machine Learning Analysis

Pearson pairwise correlation values were computed to assess the relationships between all of the features. To explain the relationship between the input features and the output, SHAP (SHapley Additive exPlanations) TreeExplainer analysis[57] was used. SHAP shows the importance of the input features in the output prediction. SHAP analysis is performed with a Random Forest (RF) model trained on all of the experimental data on MNPs. For each target property, a separate RF model is trained to ensure property-specific feature importance analysis. The average values from three replicate experiments were used for each RF model, reducing 540 data points to 180 data points per property. Using different models (Gaussian Process Regression (GPR), Neural Networks (NN)) did not give any major differences in mean absolute error (MAE) values of validation and test sets in a 70−15−15 train-validation-test random split. SHAP values were visualized with different input features to identify correlations between assigned SHAP values and a feature based on another feature. The input features used for the model are as follows: mRNA payload, N/P ratio, corona length, partition coefficient (cLogP) of the protonated cationic moieties, volume of the cationic group, pK_a of the cations, log micelleplex size (determined using OptiMEM), and micelle−mRNA binding strength. All of the features (except mRNA payload, N/P ratio, and corona length) are scaled using MinMaxScaler. The Scikit-learn package[73] was used to build the RF and GPR models and PyTorch[74] was used to build the NN model. The default hyperparameters were used for the RF model, and changing the parameters did not affect our results For each input feature, a mean absolute SHAP value across all samples (normalized to the highest mean absolute SHAP value for each output variable) is calculated to assess the average importance of each feature for a given data point. A high mean absolute SHAP value would correspond to an important feature and vice versa. The model is trained on all data points where mRNA dosage is 0.5 μg and the N/P ratio is 10 (Train R^2 = 0.985).

■ ASSOCIATED CONTENT

Supporting Information

The Supporting Information is available free of charge at https://pubs.acs.org/doi/10.1021/jacsau.5c00084.

> Polymer synthesis and characterization information in the form of NMR spectra, SEC traces, and potentiometric titrations; micelle and micelleplex DLS characterization data; detailed biophysical characterization data (dye exclusion assay, DLS aggregation data); expanded transfection data; detailed internalization data; cell apoptosis/necrosis data; gating schemes; Baf-A1 assays; serum transfection; machine learning; and *in vivo* mouse experiments. (PDF)

■ AUTHOR INFORMATION

Corresponding Author

Theresa M. Reineke − *Department of Chemistry, University of Minnesota, Minneapolis, Minnesota 55455, United States;* orcid.org/0000-0001-7020-3450; Email: treineke@umn.edu

Authors

Sidharth Panda − *Department of Chemistry, University of Minnesota, Minneapolis, Minnesota 55455, United States;* orcid.org/0000-0002-3856-6240

Ella J. Eaton − *Department of Genetics, Cell Biology and Development, Department of Pediatrics, and Masonic Cancer Center, University of Minnesota, Minneapolis, Minnesota 55455, United States; Center for Genome Engineering, University of Minnesota, Minneapolis, Minnesota 55455, United States*

Praveen Muralikrishnan − *Department of Chemical Engineering and Materials Science, University of Minnesota, Minneapolis, Minnesota 55455, United States*

Erin M. Stelljes − *Department of Pediatrics, University of Minnesota, Minneapolis, Minnesota 55455, United States*

Davis Seelig − *Department of Veterinary Clinical Sciences, College of Veterinary Medicine, University of Minnesota, Saint Paul, Minnesota 55108, United States*

Michael C. Leyden − *Department of Chemical Engineering and Materials Science, University of Minnesota, Minneapolis, Minnesota 55455, United States*

Alexandria K. Gilkey − *Department of Pediatrics, University of Minnesota, Minneapolis, Minnesota 55455, United States*

Jackson T. Barnes − *Department of Genetics, Cell Biology and Development, University of Minnesota, Minneapolis, Minnesota 55455, United States*

David V. Morrissey − *Pfizer Research and Development, Cambridge, Massachusetts 02139, United States*

Sapna Sarupria − *Department of Chemistry, University of Minnesota, Minneapolis, Minnesota 55455, United States;* orcid.org/0000-0001-7692-8313

Branden S. Moriarity − *Department of Pediatrics and Masonic Cancer Center, University of Minnesota, Minneapolis, Minnesota 55455, United States; Center for Genome Engineering, University of Minnesota, Minneapolis, Minnesota 55455, United States*

Complete contact information is available at: https://pubs.acs.org/10.1021/jacsau.5c00084

Author Contributions

The manuscript was written through contributions of all authors. All authors have given approval to the final version of the manuscript.

Notes

The authors declare no competing financial interest.

■ ACKNOWLEDGMENTS

Funding for this research was provided by Pfizer. This work was supported by the resources and staff at the University of Minnesota University Imaging Centers (UIC) (SCR_020997, NIH grant 1S10OD032261) and University of Minnesota Research Animal Resources (RAR). Figures were created in part with BioRender.com.

■ REFERENCES

(1) Damha, M. J. Exciting Times in the Field of Nucleic Acid Therapeutics. *Trends Mol. Med.* **2019**, *25* (12), 1051−1052.

(2) Lin, J.; Wang, X.; Ni, D.; Chen, Y.; Chen, C.; Liu, Y. Combinational Gene Therapy toward Cancer with Nanoplatform: Strategies and Principles. *ACS Mater. Au* **2023**, *3* (6), 584−599.

(3) Kulkarni, J. A.; Witzigmann, D.; Thomson, S. B.; Chen, S.; Leavitt, B. R.; Cullis, P. R.; van der Meel, R. The Current Landscape of Nucleic Acid Therapeutics. *Nat. Nanotechnol.* **2021**, *16* (6), 630−643.

(4) ASGCT − American Society of Gene & Cell Therapy. Landscape Report. https://www.asgct.org/publications/landscape-report (accessed September 22, 2024).

(5) Thomas, S. J.; Moreira, E. D.; Kitchin, N.; Absalon, J.; Gurtman, A.; Lockhart, S.; Perez, J. L.; Marc, G. P.; Polack, F. P.; Zerbini, C.; Bailey, R.; Swanson, K. A.; Xu, X.; Roychoudhury, S.; Koury, K.; Bouguermouh, S.; Kalina, W. V.; Cooper, D.; Frenck, R. W.; Hammitt, L. L.; Türeci, Ö.; Nell, H.; Schaefer, A.; Ünal, S.; Yang, Q.; Liberator, P.; Tresnan, D. B.; Mather, S.; Dormitzer, P. R.; Şahin, U.; Gruber, W. C.; Jansen, K. U. Safety and Efficacy of the BNT162b2 mRNA Covid-19 Vaccine through 6 Months. *N. Engl. J. Med.* **2021**, *385* (19), 1761−1773.

(6) Shroff, R. T.; Chalasani, P.; Wei, R.; Pennington, D.; Quirk, G.; Schoenle, M. V.; Peyton, K. L.; Uhrlaub, J. L.; Ripperger, T. J.; Jergović, M.; Dalgai, S.; Wolf, A.; Whitmer, R.; Hammad, H.; Carrier, A.; Scott, A. J.; Nikolich-Žugich, J.; Worobey, M.; Sprissler, R.; Dake, M.; LaFleur, B. J.; Bhattacharya, D. Immune Responses to Two and Three Doses of the BNT162b2 mRNA Vaccine in Adults with Solid Tumors. *Nat. Med.* **2021**, *27* (11), 2002−2011.

(7) Hou, X.; Zaks, T.; Langer, R.; Dong, Y. Lipid Nanoparticles for mRNA Delivery. *Nat. Rev. Mater.* **2021**, *6* (12), 1078−1094.

(8) Wadhwa, A.; Aljabbari, A.; Lokras, A.; Foged, C.; Thakur, A. Opportunities and Challenges in the Delivery of mRNA-Based Vaccines. *Pharmaceutics* **2020**, *12* (2), 102.

(9) Crommelin, D. J. A.; Anchordoquy, T. J.; Volkin, D. B.; Jiskoot, W.; Mastrobattista, E. Addressing the Cold Reality of mRNA Vaccine Stability. *J. Pharm. Sci.* **2021**, *110* (3), 997−1001.

(10) Buck, J.; Grossen, P.; Cullis, P. R.; Huwyler, J.; Witzigmann, D. Lipid-Based DNA Therapeutics: Hallmarks of Non-Viral Gene Delivery. *ACS Nano* **2019**, *13* (4), 3754−3782.

(11) Thomas, C. E.; Ehrhardt, A.; Kay, M. A. Progress and Problems with the Use of Viral Vectors for Gene Therapy. *Nat. Rev. Genet.* **2003**, *4* (5), 346−358.

(12) Bouard, D.; Alazard-Dany, D.; Cosset, F.-L. Viral Vectors: From Virology to Transgene Expression. *Br. J. Pharmacol.* **2009**, *157* (2), 153−165.

(13) Kumar, R.; Santa Chalarca, C. F.; Bockman, M. R.; Bruggen, C. V.; Grimme, C. J.; Dalal, R. J.; Hanson, M. G.; Hexum, J. K.; Reineke, T. M. Polymeric Delivery of Therapeutic Nucleic Acids. *Chem. Rev.* **2021**, *121* (18), 11527−11652.

(14) Yang, W.; Mixich, L.; Boonstra, E.; Cabral, H. Polymer-Based mRNA Delivery Strategies for Advanced Therapies. *Adv. Healthcare Mater.* **2023**, *12* (15), No. 2202688.

(15) Demeneix, B.; Behr, J. Polyethylenimine (PEI). *Adv. Genet.* **2005**, *53*, 215−230, DOI: 10.1016/S0065-2660(05)53008-6.

(16) Shim, B.-S.; Park, S.-M.; Quan, J.-S.; Jere, D.; Chu, H.; Song, M. K.; Kim, D. W.; Jang, Y.-S.; Yang, M.-S.; Han, S. H.; Park, Y.-H.; Cho, C.-S.; Yun, C.-H. Intranasal Immunization with Plasmid DNA Encoding Spike Protein of SARS-Coronavirus/Polyethylenimine Nanoparticles Elicits Antigen-Specific Humoral and Cellular Immune Responses. *BMC Immunol.* **2010**, *11* (1), 65.

(17) Démoulins, T.; Ebensen, T.; Schulze, K.; Englezou, P. C.; Pelliccia, M.; Guzmán, C. A.; Ruggli, N.; McCullough, K. C. Self-Replicating RNA Vaccine Functionality Modulated by Fine-Tuning of Polyplex Delivery Vehicle Structure. *J. Controlled Release* **2017**, *266*, 256−271.

(18) Levačić, A. K.; Berger, S.; Müller, J.; Wegner, A.; Lächelt, U.; Dohmen, C.; Rudolph, C.; Wagner, E. Dynamic mRNA Polyplexes Benefit from Bioreducible Cleavage Sites for *in Vitro* and *in Vivo* Transfer. *J. Controlled Release* **2021**, *339*, 27−40.

(19) Convertine, A. J.; Diab, C.; Prieve, M.; Paschal, A.; Hoffman, A. S.; Johnson, P. H.; Stayton, P. S. pH-Responsive Polymeric Micelle Carriers for siRNA Drugs. *Biomacromolecules* **2010**, *11* (11), 2904−2911.

(20) Fliervoet, L. A. L.; Zhang, H.; van Grossen, E.; Fortuin, K.; Duin, N. J. C. B.; Remaut, K.; Schiffelers, R. M.; Hennink, W. E.; Vermonden, T. Local Release of siRNA Using Polyplex-Loaded Thermosensitive Hydrogels. *Nanoscale* **2020**, *12* (18), 10347−10360.

(21) Ulkoski, D.; Munson, M. J.; Jacobson, M. E.; Palmer, C. R.; Carson, C. S.; Sabirsh, A.; Wilson, J. T.; Krishnamurthy, V. R. High-Throughput Automation of Endosomolytic Polymers for mRNA Delivery. *ACS Appl. Bio Mater.* **2021**, *4* (2), 1640−1654.

(22) Kataoka, K.; Harada, A.; Nagasaki, Y. Block Copolymer Micelles for Drug Delivery: Design, Characterization and Biological Significance. *Adv. Drug Delivery Rev.* **2012**, *64*, 37−48.

(23) Pereira, P.; Barreira, M.; Queiroz, J. A.; Veiga, F.; Sousa, F.; Figueiras, A. Smart Micelleplexes as a New Therapeutic Approach for RNA Delivery. *Expert Opin. Drug Delivery* **2017**, *14* (3), 353−371.

(24) Pereira-Silva, M.; Jarak, I.; Alvarez-Lorenzo, C.; Concheiro, A.; Santos, A. C.; Veiga, F.; Figueiras, A. Micelleplexes as Nucleic Acid Delivery Systems for Cancer-Targeted Therapies. *J. Controlled Release* **2020**, *323*, 442−462.

(25) Sinani, G.; Durgun, M. E.; Cevher, E.; Özsoy, Y. Polymeric-Micelle-Based Delivery Systems for Nucleic Acids. *Pharmaceutics* **2023**, *15* (8), 2021.

(26) Laaser, J. E.; Lohmann, E.; Jiang, Y.; Reineke, T. M.; Lodge, T. P. Architecture-Dependent Stabilization of Polyelectrolyte Complexes between Polyanions and Cationic Triblock Terpolymer Micelles. *Macromolecules* **2016**, *49* (17), 6644−6654.

(27) Jiang, Y.; Lodge, T. P.; Reineke, T. M. Packaging pDNA by Polymeric ABC Micelles Simultaneously Achieves Colloidal Stability and Structural Control. *J. Am. Chem. Soc.* **2018**, *140* (35), 11101−11111.

(28) Laaser, J. E.; Jiang, Y.; Petersen, S. R.; Reineke, T. M.; Lodge, T. P. Interpolyelectrolyte Complexes of Polycationic Micelles and Linear Polyanions: Structural Stability and Temporal Evolution. *J. Phys. Chem. B* **2015**, *119* (52), 15919−15928.

(29) Tan, Z.; Jiang, Y.; Zhang, W.; Karls, L.; Lodge, T. P.; Reineke, T. M. Polycation Architecture and Assembly Direct Successful Gene Delivery: Micelleplexes Outperform Polyplexes via Optimal DNA Packaging. *J. Am. Chem. Soc.* **2019**, *141* (40), 15804−15817.

(30) Grimme, C. J.; Hanson, M. G.; Corcoran, L. G.; Reineke, T. M. Polycation Architecture Affects Complexation and Delivery of Short Antisense Oligonucleotides: Micelleplexes Outperform Polyplexes. *Biomacromolecules* **2022**, *23* (8), 3257−3271.

(31) Santa Chalarca, C. F.; Dalal, R. J.; Chapa, A.; Hanson, M. G.; Reineke, T. M. Cation Bulk and pKa Modulate Diblock Polymer Micelle Binding to pDNA. *ACS Macro Lett.* **2022**, *11* (4), 588−594.

(32) Hanson, M. G.; Grimme, C. J.; Santa Chalarca, C. F.; Reineke, T. M. Cationic Micelles Outperform Linear Polymers for Delivery of Antisense Oligonucleotides in Serum: An Exploration of Polymer Architecture, Cationic Moieties, and Cell Addition Order. *Bioconjugate Chem.* **2022**, *33* (11), 2121−2131.

(33) Tan, Z.; Jiang, Y.; Ganewatta, M. S.; Kumar, R.; Keith, A.; Twaroski, K.; Pengo, T.; Tolar, J.; Lodge, T. P.; Reineke, T. M. Block Polymer Micelles Enable CRISPR/Cas9 Ribonucleoprotein Delivery: Physicochemical Properties Affect Packaging Mechanisms and Gene Editing Efficiency. *Macromolecules* **2019**, *52* (21), 8197−8206.

(34) Leer, K.; Reichel, L. S.; Kimmig, J.; Richter, F.; Hoeppener, S.; Brendel, J. C.; Zechel, S.; Schubert, U. S.; Traeger, A. Optimization of Mixed Micelles Based on Oppositely Charged Block Copolymers by Machine Learning for Application in Gene Delivery. *Small* **2024**, *20* (6), No. 2306116.

(35) Miteva, M.; Kirkbride, K. C.; Kilchrist, K. V.; Werfel, T. A.; Li, H.; Nelson, C. E.; Gupta, M. K.; Giorgio, T. D.; Duvall, C. L. Tuning PEGylation of Mixed Micelles to Overcome Intracellular and Systemic siRNA Delivery Barriers. *Biomaterials* **2015**, *38*, 97−107.

(36) Patel, S. S.; Hoogenboezem, E. N.; Yu, F.; DeJulius, C. R.; Fletcher, R. B.; Sorets, A. G.; Cherry, F. K.; Lo, J. H.; Bezold, M. G.; Francini, N.; d'Arcy, R.; Brasuell, J. E.; Cook, R. S.; Duvall, C. L. Core Polymer Optimization of Ternary siRNA Nanoparticles Enhances in Vivo Safety, Pharmacokinetics, and Tumor Gene Silencing. *Biomaterials* **2023**, *297*, No. 122098.

(37) Jiang, X.; Dai, H.; Ke, C.-Y.; Mo, X.; Torbenson, M. S.; Li, Z.; Mao, H.-Q. PEG-*b*-PPA/DNA Micelles Improve Transgene Expression in Rat Liver through Intrabiliary Infusion. *J. Controlled Release* **2007**, *122* (3), 297−304.

(38) Tenzer, S.; Docter, D.; Kuharev, J.; Musyanovych, A.; Fetz, V.; Hecht, R.; Schlenk, F.; Fischer, D.; Kiouptsi, K.; Reinhardt, C.; Landfester, K.; Schild, H.; Maskos, M.; Knauer, S. K.; Stauber, R. H. Rapid Formation of Plasma Protein Corona Critically Affects Nanoparticle Pathophysiology. *Nat. Nanotechnol.* **2013**, *8* (10), 772−781.

(39) Lundqvist, M.; Stigler, J.; Elia, G.; Lynch, I.; Cedervall, T.; Dawson, K. A. Nanoparticle Size and Surface Properties Determine the Protein Corona with Possible Implications for Biological Impacts. *Proc. Natl. Acad. Sci. U.S.A.* **2008**, *105* (38), 14265−14270.

(40) Bertrand, N.; Grenier, P.; Mahmoudi, M.; Lima, E. M.; Appel, E. A.; Dormont, F.; Lim, J.-M.; Karnik, R.; Langer, R.; Farokhzad, O. C. Mechanistic Understanding of in Vivo Protein Corona Formation on Polymeric Nanoparticles and Impact on Pharmacokinetics. *Nat. Commun.* **2017**, *8* (1), No. 777.

(41) Dilliard, S. A.; Cheng, Q.; Siegwart, D. J. On the Mechanism of Tissue-Specific mRNA Delivery by Selective Organ Targeting Nanoparticles. *Proc. Natl. Acad. Sci. U.S.A.* **2021**, *118* (52), No. e2109256118.

(42) Cheng, Q.; Wei, T.; Farbiak, L.; Johnson, L. T.; Dilliard, S. A.; Siegwart, D. J. Selective Organ Targeting (SORT) Nanoparticles for Tissue-Specific mRNA Delivery and CRISPR−Cas Gene Editing. *Nat. Nanotechnol.* **2020**, *15* (4), 313−320.

(43) Dilliard, S. A.; Sun, Y.; Brown, M. O.; Sung, Y.-C.; Chatterjee, S.; Farbiak, L.; Vaidya, A.; Lian, X.; Wang, X.; Lemoff, A.; Siegwart, D. J. The Interplay of Quaternary Ammonium Lipid Structure and Protein Corona on Lung-Specific mRNA Delivery by Selective Organ Targeting (SORT) Nanoparticles. *J. Controlled Release* **2023**, *361*, 361−372.

(44) Cao, Y.; He, Z.; Chen, Q.; He, X.; Su, L.; Yu, W.; Zhang, M.; Yang, H.; Huang, X.; Li, J. Helper-Polymer Based Five-Element Nanoparticles (FNPs) for Lung-Specific mRNA Delivery with Long-Term Stability after Lyophilization. *Nano Lett.* **2022**, *22* (16), 6580−6589.

(45) Ting, J. M.; Fisher, J. D.; Conyers, T.; Patil, S.; Robohn, C. G.; Tamayo-Mendoza, T.; Oviedo, F.; Murthy, S. K. Predictive Design of Multimonomeric Polyelectrolytes Enables Lung-Specific Gene Delivery. *Polym. Chem.* **2024**, *15* (26), 2627−2633.

(46) Li, H.; Cortez, M. A.; Phillips, H. R.; Wu, Y.; Reineke, T. M. Poly(2-Deoxy-2-Methacrylamido Glucopyranose)-b-Poly(Methacrylate Amine)s: Optimization of Diblock Glycopolycations for Nucleic Acid Delivery. *ACS Macro Lett.* **2013**, *2* (3), 230−235.

(47) Funhoff, A. M.; van Nostrum, C. F.; Koning, G. A.; Schuurmans-Nieuwenbroek, N. M. E.; Crommelin, D. J. A.; Hennink, W. E. Endosomal Escape of Polymeric Gene Delivery Complexes Is Not Always Enhanced by Polymers Buffering at Low pH. *Biomacromolecules* **2004**, *5* (1), 32−39.

(48) Arigita, C.; Zuidam, N. J.; Crommelin, D. J. A.; Hennink, W. E. Association and Dissociation Characteristics of Polymer/DNA Complexes Used for Gene Delivery. *Pharm. Res.* **1999**, *16* (10), 1534−1541.

(49) Gauthier, M. A.; Gibson, M. I.; Klok, H.-A. Synthesis of Functional Polymers by Post-Polymerization Modification. *Angew. Chem., Int. Ed.* **2009**, *48* (1), 48−58.

(50) Eberhardt, M.; Mruk, R.; Zentel, R.; Théato, P. Synthesis of Pentafluorophenyl(Meth)Acrylate Polymers: New Precursor Polymers for the Synthesis of Multifunctional Materials. *Eur. Polym. J.* **2005**, *41* (7), 1569−1575.

(51) Chandler, D. Interfaces and the Driving Force of Hydrophobic Assembly. *Nature* **2005**, *437* (7059), 640−647.

(52) Iqbal, S.; Blenner, M.; Alexander-Bryant, A.; Larsen, J. Polymersomes for Therapeutic Delivery of Protein and Nucleic Acid Macromolecules: From Design to Therapeutic Applications. *Biomacromolecules* **2020**, *21* (4), 1327−1350.

(53) Richter, F.; Martin, L.; Leer, K.; Moek, E.; Hausig, F.; Brendel, J. C.; Traeger, A. Tuning of Endosomal Escape and Gene Expression by Functional Groups, Molecular Weight and Transfection Medium: A Structure−Activity Relationship Study. *J. Mater. Chem. B* **2020**, *8* (23), 5026−5041.

(54) Meli, L.; Lodge, T. P. Equilibrium vs Metastability: High-Temperature Annealing of Spherical Block Copolymer Micelles in an Ionic Liquid. *Macromolecules* **2009**, *42* (3), 580−583.

(55) Mehta, M. J.; Kim, H. J.; Lim, S. B.; Naito, M.; Miyata, K. Recent Progress in the Endosomal Escape Mechanism and Chemical Structures of Polycations for Nucleic Acid Delivery. *Macromol. Biosci.* **2024**, *24* (4), No. 2300366.

(56) Padhy, A.; Das, P.; Mahadik, N. S.; Panda, S.; Anas, M.; Das, S.; Banerjee, R.; Gupta, S. S. Design and Synthesis of a Shikimoyl-Functionalized Cationic Di-Block Copolypeptide for Cancer Cell Specific Gene Transfection. *J. Mater. Chem. B* **2024**, *12* (36), 8952−8965.

(57) Lundberg, S. M.; Erion, G.; Chen, H.; DeGrave, A.; Prutkin, J. M.; Nair, B.; Katz, R.; Himmelfarb, J.; Bansal, N.; Lee, S.-I. From Local Explanations to Global Understanding with Explainable AI for Trees. *Nat. Mach. Intell.* **2020**, *2* (1), 56−67.

(58) El-Sayed, A.; Harashima, H. Endocytosis of Gene Delivery Vectors: From Clathrin-Dependent to Lipid Raft-Mediated Endocytosis. *Mol. Ther.* **2013**, *21* (6), 1118−1130.

(59) Khalil, I. A.; Kogure, K.; Akita, H.; Harashima, H. Uptake Pathways and Subsequent Intracellular Trafficking in Nonviral Gene Delivery. *Pharmacol. Rev.* **2006**, *58* (1), 32−45.

(60) Kaksonen, M.; Roux, A. Mechanisms of Clathrin-Mediated Endocytosis. *Nat. Rev. Mol. Cell Biol.* **2018**, *19* (5), 313−326.

(61) Van Bruggen, C.; Punihaole, D.; Keith, A. R.; Schmitz, A. J.; Tolar, J.; Frontiera, R. R.; Reineke, T. M. Quinine Copolymer Reporters Promote Efficient Intracellular DNA Delivery and Illuminate a Protein-Induced Unpackaging Mechanism. *Proc. Natl. Acad. Sci. U.S.A.* **2020**, *117* (52), 32919−32928.

(62) Cho, Y. W.; Kim, J.-D.; Park, K. Polycation Gene Delivery Systems: Escape from Endosomes to Cytosol. *J. Pharm. Pharmacol.* **2003**, *55* (6), 721−734.

(63) Bus, T.; Traeger, A.; Schubert, U. S. The Great Escape: How Cationic Polyplexes Overcome the Endosomal Barrier. *J. Mater. Chem. B* **2018**, *6* (43), 6904−6918.

(64) Yang, S.; May, S. Release of Cationic Polymer-DNA Complexes from the Endosome: A Theoretical Investigation of the Proton Sponge Hypothesis. *J. Chem. Phys.* **2008**, *129* (18), No. 185105.

(65) Kichler, A.; Leborgne, C.; Coeytaux, E.; Danos, O. Polyethylenimine-Mediated Gene Delivery: A Mechanistic Study. *J. Gene Med.* **2001**, *3* (2), 135−144.

(66) Bowman, E. J.; Siebers, A.; Altendorf, K. Bafilomycins: A Class of Inhibitors of Membrane ATPases from Microorganisms, Animal Cells, and Plant Cells. *Proc. Natl. Acad. Sci. U.S.A.* **1988**, *85* (21), 7972−7976.

(67) Sprouse, D.; Reineke, T. M. Investigating the Effects of Block versus Statistical Glycopolycations Containing Primary and Tertiary Amines for Plasmid DNA Delivery. *Biomacromolecules* **2014**, *15* (7), 2616−2628.

(68) van Engeland, M.; Nieland, L. J. W.; Ramaekers, F. C. S.; Schutte, B.; Reutelingsperger, C. P. M. Annexin V-Affinity Assay: A Review on an Apoptosis Detection System Based on Phosphatidylserine Exposure. *Cytometry* **1998**, *31* (1), 1−9.

(69) Su, K.; Shi, L.; Sheng, T.; Yan, X.; Lin, L.; Meng, C.; Wu, S.; Chen, Y.; Zhang, Y.; Wang, C.; Wang, Z.; Qiu, J.; Zhao, J.; Xu, T.; Ping, Y.; Gu, Z.; Liu, S. Reformulating Lipid Nanoparticles for Organ-Targeted mRNA Accumulation and Translation. *Nat. Commun.* **2024**, *15* (1), No. 5659.

(70) Baharom, F.; Rankin, G.; Blomberg, A.; Smed-Sörensen, A. Human Lung Mononuclear Phagocytes in Health and Disease. *Front. Immunol.* **2017**, *8*, 499.

(71) Tanaka, T.; Narazaki, M.; Kishimoto, T. IL-6 in Inflammation, Immunity, and Disease. *Cold Spring Harb. Perspect. Biol.* **2014**, *6* (10), No. a016295.

(72) Balandat, M.; Karrer, B.; Jiang, D. R.; Daulton, S.; Letham, B.; Wilson, A. G.; Bakshy, E. BOTORCH: A Framework for Efficient Monte-Carlo Bayesian Optimization. In *Proceedings of the 34th International Conference on Neural Information Processing Systems; NIPS'20*; Curran Associates Inc.: Red Hook, NY, USA, 2020.

(73) Prettenhofer, P.; Weiss, R.; Dubourg, V.; Vanderplas, J.; Passos, A.; Cournapeau, D.; Brucher, M.; Perrot, M.; Duchesnay, E. Scikit-Learn: Machine Learning in Python. *J. Mach. Learn. Res.* **2011**, *12*, 2825−2830.

(74) Paszke, A.; Gross, S.; Massa, F.; Lerer, A.; Bradbury, J.; Chanan, G.; Killeen, T.; Lin, Z.; Gimelshein, N.; Antiga, L.; Desmaison, A.; Kopf, A.; Yang, E.; DeVito, Z.; Raison, M.; Tejani, A.; Chilamkurthy, S.; Steiner, B.; Fang, L.; Bai, J.; Chintala, S. PyTorch: An Imperative Style, High-Performance Deep Learning Library. In *Advances in Neural Information Processing Systems*; Curran Associates, Inc., 2019; Vol. 32.